Monitoring SARS-CoV-2 infection using a double reporter-expressing virus

Kevin Chiem[1], Jun-Gyu Park[1], Desarey Morales Vasquez[1], Richard K. Plemper[2], Jordi B. Torrelles[1], James J. Kobie[3], Mark R. Walter[4], Chengjin Ye[1*], Luis Martinez-Sobrido[1*]

[1] Texas Biomedical Research Institute, San Antonio, Texas 78227, USA

[2] Center for Translational Antiviral Research, Institute for Biomedical Sciences, Georgia State University, Atlanta, GA, USA

[3] Department of Medicine, Division of Infectious Diseases, University of Alabama at Birmingham, Birmingham, Alabama 35294, USA

[4] Department of Microbiology, University of Alabama at Birmingham, Birmingham, Alabama 35294, USA

*Lead contact email and correspondence:

cye@txbiomed.org

lmartinez@txbiomed.org

Running title: A double reporter-expressing recombinant SARS-CoV-2

ABSTRACT

Severe acute respiratory syndrome coronavirus 2 (SARS-CoV-2) is the highly contagious agent responsible for the coronavirus disease 2019 (COVID-19) pandemic. An essential requirement for understanding SARS-CoV-2 fundamental biology and the impact of anti-viral therapeutics are robust methods to detect for the presence of the virus in infected cells or animal models. Despite the development and successful generation of recombinant (r)SARS-CoV-2 expressing fluorescent or luciferase reporter genes, knowledge acquired from their use in *in vitro* assays and/or in live animals are limited to the properties of the fluorescent or luciferase reporter genes. Herein, for the first time, we engineered a replication-competent rSARS-CoV-2 that expresses both fluorescent (mCherry) and luciferase (Nluc) reporter genes (rSARS-CoV-2/mCherry-Nluc) to overcome limitations associated with the use of a single reporter gene. In cultured cells, rSARS-CoV-2/mCherry-Nluc displayed similar viral fitness as rSARS-CoV-2 expressing single reporter fluorescent and luciferase genes (rSARS-CoV-2/mCherry and rSARS-CoV-2/Nluc, respectively), or wild-type (WT) rSARS-CoV-2, while maintaining comparable expression levels of both reporter genes. *In vivo*, rSARS-CoV-2/mCherry-Nluc has similar pathogenicity in K18 human angiotensin converting enzyme 2 (hACE2) transgenic mice than rSARS-CoV-2 expressing individual reporter genes, or WT rSARS-CoV-2. Importantly, rSARS-CoV-2/mCherry-Nluc facilitates the assessment of viral infection and transmission in golden Syrian hamsters using *in vivo* imaging systems (IVIS). Altogether, this study demonstrates the feasibility of using this novel bireporter-expressing rSARS-CoV-2 for the study SARS-CoV-2 *in vitro* and *in vivo*.

IMPORTANCE

Despite the availability of vaccines and antivirals, the coronavirus disease 2019 (COVID-19) pandemic caused by Severe Acute Respiratory Syndrome Coronavirus 2 (SARS-CoV-2) continues to ravage health care institutions worldwide. Previously, we have generated replication-competent recombinant (r)SARS-CoV-2 expressing fluorescent or luciferase reporter proteins to track viral infection *in vitro* and/or *in vivo*. However, these rSARS-CoV-2 are restricted to express only a single fluorescent or a luciferase reporter gene, limiting or preventing their use to specific *in vitro* assays and/or *in vivo* studies. To overcome this limitation, we have engineered a rSARS-CoV-2 expressing both fluorescent (mCherry) and luciferase (Nluc) genes and demonstrated its feasibility to study the biology of SARS-CoV-2 *in vitro* and/or *in vivo*, including the identification and characterization of neutralizing antibodies and/or antivirals. Using rodent models, we visualize SARS-CoV-2 infection and transmission through *in vivo* imaging systems (IVIS).

INTRODUCTION

Severe acute respiratory syndrome coronavirus 2 (SARS-CoV-2) is responsible for the coronavirus disease 2019 (COVID-19) pandemic (1). Since the first reported case in Wuhan, China, SARS-CoV-2 has spread worldwide and has been associated with more than 500 million confirmed cases and over 6 million deaths (https://coronavirus.jhu.edu/map.html) (2), in part due to its innate high transmissibility (3, 4). In the past two decades, two other human coronaviruses have being responsible for severe disease in humans, including severe acute respiratory syndrome coronavirus (SARS-CoV) in 2002 and the Middle East respiratory syndrome coronavirus (MERS-CoV) in 2012 (5, 6). Further, four endemic human coronaviruses are responsible for common cold-like respiratory disease: OC43, NL63, 229E, and HKU1 (7, 8). A unique feature of SARS-CoV-2 compared to known betacoronaviruses is the addition of a furin cleavage site in the viral spike (S) glycoprotein which is a major contributor to the virus's increased transmissibility and pathogenicity (9, 10). Several prophylactic (vaccines) and therapeutic (antivirals or monoclonal antibodies) options have been approved by the United States (US) Food and Drug Administration (FDA) to prevent or treat, respectively, SARS-CoV-2 infection. These include three vaccines [Spikevax (former Moderna), COMIRNATY (former BioNTech & Pfizer), and Janssen], several therapeutic antiviral drugs (remdesivir, baricitinib, molnupiravir, and paxlovid) and one monoclonal antibody (MAb, bamlanivimab) (11-13). Unfortunately, SARS-CoV-2 has rapidly accumulated mutations, leading to the emergence of variants of concern (VoC) and variants of interest (VoI) jeopardizing the effectiveness of existing preventive and/or treatment options (14-18).

Reverse genetics systems have permitted the generation of recombinant RNA viruses entirely from cloned cDNA, facilitating studies to better understand multiple aspects of the biology of viruses, including, among others, mechanisms of viral infection, pathogenesis, transmission, and disease (19-29). Another application of reverse genetics is the generation of recombinant viruses containing gene mutations and/or deletions that result in viral attenuation for their implementation as safe, immunogenic, and protective live-attenuated vaccines (LAV) (20, 30-35). Moreover, reverse genetics have been used to generate recombinant viruses expressing reporter proteins, thereby abolishing the need of secondary approaches for viral detection (36-42). In this regard, genetically modified recombinant viruses expressing reporter genes have been generated to monitor viral infection in cultured cells and/or in animal models using reporter expression as a valid surrogate readout for viral infection (36, 43-47). Notably, these reporter-expressing viruses have the potential to be used in high-throughput screening (HTS) settings to identify antivirals or neutralizing antibodies that can inhibit or neutralize, respectively, viral infection; and to visualize the dynamics of viral infection in validated animal models using *in vivo* imaging systems (IVIS).

Fluorescent and luciferase proteins are used to generate reporter-expressing viruses and represent ideal choices due to their high sensitivity and stability (48-54). Since these reporter genes have dissimilar characteristics, their selection is largely motivated by the type of study or application. Fluorescent proteins are easily detected when excited by absorbing energy at a particular wavelength, which is subsequently emitted as light at higher wavelength as the molecules drop to a lesser energy state (53). Hence, reporter viruses expressing fluorescent proteins are typically used for *in vitro* studies to observe

cellular localization and/or to identify the presence of infected cells (25, 36, 37, 45, 55). Moreover, fluorescence-expressing recombinant viruses are used to identify the presence of the virus in infected cells in validated animal models using *ex vivo* imaging (36, 37, 43-45). However, *in vivo*, fluorescent signals are often obscured by autofluorescence and have insufficient detection due to light scattering. Conversely, luciferases produce bright and localized signals in live organisms to be monitored in real-time using IVIS and represent a viable surrogate of viral replication (36, 37, 56). Moreover, viruses expressing luciferase genes are more sensitive and convenient for quantitative analyses compared to their fluorescent-expressing counterparts (37, 43, 46). Despite the clear advantages of both fluorescence and luciferase reporter genes, only recombinant viruses expressing either fluorescent or luciferase reporter genes have been previously described in the literature (36, 43, 44, 46, 47). In the past, we overcame this issue by generating dual reporter viruses expressing both luciferase and fluorescent reporter genes and demonstrated its advantages with influenza and vaccinia viruses (36, 37, 56).

In this study, we used our previously described bacterial artificial chromosome (BAC)-based reverse genetics (20, 21, 57-59) and the innovative 2A approach (43, 44) to pioneer a rSARS-CoV-2 expressing both fluorescence mCherry and luciferase Nluc reporter genes (rSARS-CoV-2/mCherry-Nluc). Our results demonstrate that rSARS-CoV-2/mCherry-Nluc has similar properties in cultured cells than rSARS-CoV-2 expressing individual mCherry or Nluc reporter genes, or wild-type (WT) rSARS-CoV-2. Importantly expression of the double mCherry-Nluc reporter gene did not affect viral replication or pathogenesis in K18 human angiotensin converting enzyme 2 (hACE2) transgenic mice or golden Syrian hamsters, validating its use for both *in vitro* and/or *in vivo* studies.

MATERIAL AND METHODS

Biosafety and ethics statement

In vitro and *in vivo* experiments involving infectious rSARS-CoV-2 were conducted in a biosafety level 3 (BSL3) laboratory at Texas Biomedical Research Institute. Experimental procedures involving cell culture and animal studies were approved by the Texas Biomedical Research Institute Biosafety and Recombinant DNA Committees (BSC and RDC, respectively) and the Institutional Animal Care and Use Committee (IACUC).

Cells and viruses

African green monkey kidney epithelial cells (Vero E6; CRL-1586) were propagated and maintained in Dulbecco's modified Eagle's medium (DMEM; Corning) supplemented with 5% fetal bovine serum (FBS; VWR) and 1% PSG (100 U/ml penicillin, 100 µg/ml streptomycin, and 2 mM L-glutamine; Corning) at 37°C with 5% CO_2.

Recombinant (r)SARS-CoV-2 were generated based on the whole genomic sequence of the USA-WA1/2020 (WA-1) strain (accession no. MN985325) (43, 58) using a previously described bacterial artificial chromosome (BAC)-based reverse genetics system (20, 21, 57-59). Viral titers (plaque forming units per milliliter, PFU/ml) were determined by plaque assay in Vero E6 cells.

Rescue of recombinant double reporter-expressing SARS-CoV-2

A BAC plasmid was used for the rescue of rSARS-CoV-2 expressing mCherry and Nanoluciferase (Nluc), referred as rSARS-CoV-2/mCherry-Nluc, as previously described (43). Briefly, a fused version of mCherry and Nluc was inserted in front of the viral N protein gene along with a porcine teschovirus 1 (PTV-1) 2A autocleavage site, within the pBeloBAC11 plasmid (NEB) containing the whole genomic sequence of SARS-CoV-2

WA-1 strain. We chose mCherry because red fluorescent proteins are more readily detectable in biological tissues, enabling lower absorbance and scattering of light, as well as less autofluorescence (45, 60-62). We selected Nluc due to its small size, ATP independence, and greater sensitivity and brightness compared with other luciferases (43, 46, 48, 63). Vero E6 cells (1.2 x 10^6 cells/well, 6-well plate format, triplicates) were transfected in suspension with 4.0 µg/well of SARS-CoV-2/mCherry-Nluc BAC plasmid using Lipofectamine 2000 (Thermo Fisher Scientific). Transfection media was changed to post-infection media (DMEM containing 2% FBS and 1% PSG) after 24 h, and cells were split and seeded into T75 flasks 2-days post-transfection. After 3 days, viral rescues were detected by fluorescence microscopy, and cell culture supernatants were collected, labeled as P0 and stored at -80ºC. After viral titration, P1 viral stocks were generated by infecting fresh Vero E6 cells at low multiplicity of infection (MOI) 0.0001 for 3 days and following stored at -80°C.

Reverse transcription (RT)-PCR

Total RNA was extracted from rSARS-CoV-2/mCherry-Nluc-infected (MOI 0.01) Vero E6 cells (1.2 x 10^6 cells/well, 6-well format) using TRIzol reagent (Thermo Fisher Scientific) based on the manufacturer's instructions. The viral genome between 27,895-29,534 nucleotides based on the SARS-CoV-2 WA-1 strain was RT-PCR amplified using Super Script II Reverse transcriptase (Thermo Fisher Scientific) and Expanded High Fidelity PCR system (Sigma Aldrich). Amplified DNA products were separated on a 0.7% agarose gel, purified using a Wizard Genomic DNA Purification kit (Promega), and sent for Sanger sequencing (ACGT). Primer sequences are available upon request.

Deep sequencing

RNA sequencing library was prepared with a KAPA RNA HyperPrep kit, involving 100 ng of viral RNA and 7 mM of adaptor, and was subjected to 45 min adaptor ligation incubation and 6 cycles of PCR. An Illumina Hiseq X was used to sequence all samples and raw sequencing reads were trimmed and filtered using Trimmomatic V0.32 (64, 65). Bowtie2 V2.4.1 (66) and MosDepth V0.2.6 (67) were used to map sequence reads and quantify genome coverage to reference SARS-CoV-2-WA1/2020 viral genome (MN985325.1), respectively. LoFreq V2.1.3.1 (68) was used to determine low frequency variants and eliminate sites that were less than 100 read depth or less than 1% allele frequencies.

Immunofluorescence assays

Vero E6 cells (1.2 x 10^6 cells/well, 6-well format, triplicates) were mock-infected or infected (MOI 0.01) with rSARS-CoV-2/WT, rSARS-CoV-2/mCherry, rSARS-CoV-2/Nluc, or rSARS-CoV-2/mCherry-Nluc. At 24 h post-infection (hpi), cells were fixed in 10% neutral buffered formalin at 4ºC overnight and permeabilized using 0.5% Triton X-100 in phosphate-buffered saline (PBS) for 10 min at room temperature (RT). Cells were washed with PBS, blocked with 2.5% bovine albumin serum (BSA) in PBS for 1 h and then incubated with 1 µg/ml of SARS-CoV anti-N monoclonal antibody (MAb) 1C7C7 in 1% BSA at 4ºC overnight. Cells were washed with PBS and incubated with a fluorescein isothiocyanate (FITC)-conjugated goat anti-mouse IgG (Dako; 1:200). Cell nuclei were stained with 4', 6'-diamidino-2-phenylindole (DAPI; Research Organics). Representative images (20X) were acquired using an EVOS M5000 imaging system (Thermo Fisher Scientific).

SDS-PAGE and Western blot

Cell lysates were prepared from either mock- or virus-infected (MOI 0.01) Vero E6 cells (1.2 x 10^6 cells/well, 6-well format) after 24 hpi using passive lysis buffer (Promega) based on the manufacturer's instructions. After centrifugation (12,000 x *g*) at 4ºC for 30 min, proteins were separated with 12% SDS-PAGE and transferred to nitrocellulose membranes. Membranes were blocked for 1 h with 5% dried skim milk in 0.1% Tween 20 PBS (T-PBS) and incubated at 4ºC overnight with the following specific primary MAbs or polyclonal antibodies (PAbs): N (mouse MAb 1C7C7), mCherry (rabbit Pab; Raybiotech), and Nluc (rabbit Pab, Promega). Then, membranes were incubated at 37ºC for 1 h with goat anti-mouse IgG StarBright Blue 520 or anti-rabbit IgG Starbright Blue 700 (Bio-Rad) secondary antibodies. Tubulin was used as a loading control using anti-tubulin hFAB rhodamine antibody (Bio-Rad). Proteins were detected using a ChemiDoc MP imaging system (Bio-Rad).

Plaque assay

Vero E6 cells (2 x 10^5 cells/well, 24-well plate format, triplicates) were infected with 25-50 PFUs of rSARS-CoV-2/WT, rSARS-CoV-2/mCherry, rSARS-CoV-2/Nluc, or rSARS-CoV-2/mCherry-Nluc for 1 h, overlaid with post-infection media containing 0.6% agar (Oxoid) and incubated at 37ºC in a 5% CO_2 incubator. At 72 hpi, cells were fixed in 10% neutral buffered formalin at 4ºC overnight and then mCherry-positive plaques were visualized using a ChemiDoc MP imaging system (Bio-Rad). Afterwards, cells were permeabilized in T-PBS for 10 min at RT, blocked in 2.5% BSA in PBS for 1 h, and incubated with specific primary MAb or PAb against the viral N protein (mouse MAb 1C7C7) or Nluc (rabbit PAb). To detect Nluc-positive viral plaques, cells were stained with a FITC-conjugated goat anti-rabbit IgG (Dako; 1:200) and visualized using a ChemiDoc

MP imaging system (Bio-Rad). Next, viral plaques were stained with an anti-mouse Vectastain ABC kit and DAB HRP Substrate kit (Vector laboratories) following the manufacturers' recommendations.

Viral growth kinetics

Vero E6 cells (1.2 x 10^6 cells/well, 6-well plate format, triplicates) were infected (MOI 0.01) with rSARS-CoV-2/WT, rSARS-CoV-2/mCherry, rSARS-CoV-2/Nluc, or rSARS-CoV-2/mCherry-Nluc. After 1 h adsorption, cells were washed with PBS and incubated at 37ºC in post-infection media. Viral titers in cell culture supernatants at each of the indicated time points (12, 24, 48, 72, and 96 hpi) were determined by plaque assay as described above. At each time point, mCherry expression was visualized with an EVOS M5000 imaging system. Nluc activity in the cell culture supernatants at the same times post-infection was quantified using a microplate reader and a Nano-Glo Luciferase Assay system (Promega) following the manufacturers' recommendations. Mean values and standard deviation (SD) were calculated with Microsoft Excel software.

Reporter-based microneutralization and antiviral assays

Microneutralization and antiviral assays were performed as previously described (45, 69). Human MAb 1212C2 (70) against the Spike protein receptor-binding domain (RBD) of SARS-CoV-2 was serially diluted (3-fold) in post-infection media (starting concentration of 500 ng), combined with 100-200 PFUs/well of rSARS-CoV-2/WT, rSARS-CoV-2/mCherry, rSARS-CoV-2/Nluc, or rSARS-CoV-2/mCherry-Nluc and incubated at RT for 1 h. Then, Vero E6 cells (4 x 10^4 cells/well, 96-well plate format, quadruplicates) were infected with the antibody-virus mixture and incubated at 37ºC in a 5% CO_2 incubator. Cells infected with rSARS-CoV-2/WT were overlaid with 1% Avicel as previously

described (69). Nluc activity in cell culture supernatants of cells infected with rSARS-CoV-2/Nluc or rSARS-CoV-2/mCherry-Nluc was quantified at 24 hpi using Nano-Glo luciferase substrate as per manufacturer's instructions, and a Synergy LX microplate reader and analyzed using a Gen5 data analysis software (Bio-Tek). To measure mCherry signal, cells infected with rSARS-CoV-2/mCherry or rSARS-CoV-2/mCherry-Nluc were fixed in 10% neutral buffered formalin overnight and washed with PBS before quantified in a Synergy LX microplate reader. For cells infected with rSARS-CoV-2/WT, plaques were detected using the anti-N MAb 1C7C7 as indicated above and quantified using an ImmunoSpot Analyzer (CTL). Total viral infection (100%) was determined from the number of plaques, fluorescence and luciferase values obtained from virus-infected cells without the 1212C2 hMAb. Viral infection means and SD values were calculated from quadruplicate individual wells of three independent experiments with Microsoft Excel software. Non-linear regression curves and 50% neutralization titer (NT_{50}) values were determined using GraphPad Prism Software (San Diego, CA, USA, V. 8.2.1).

Inhibition of SARS-CoV-2 in antiviral assays was conducted as previously described (45, 69). Briefly, Vero E6 cells (4 x 10^4 cells/well, 96-well plate format, quadruplicates) were infected with 100-200 PFUs/well of rSARS-CoV-2/WT, rSARS-CoV-2/mCherry, rSARS-CoV-2/Nluc, or rSARS-CoV-2/mCherry-Nluc and incubated at 37ºC for 1 h. Afterwards, the virus inoculum was removed and replaced with post-infection media containing 3-fold serial dilutions of remdesivir (starting concentration of 100 µM) and cells were incubated at 37ºC in a 5% CO_2 incubator. Cells infected with rSARS-CoV-2/WT were overlaid with 1% Avicel as previously described (69). After 24 hpi, Nluc activity from cell culture supernatants infected with rSARS-CoV-2/Nluc or rSARS-CoV-2/mCherry-

Nluc was determined using Nano-Glo luciferase substrate and a Synergy LX microplate reader. For cells infected with rSARS-CoV-2/mCherry or rSARS-CoV-2/mCherry-Nluc, mCherry expression was quantified in a Synergy LX microplate reader. Lastly, rSARS-CoV-2/WT was detected using the anti-N MAb 1C7C7 and quantified using an ImmunoSpot Analyzer (CTL). Total viral infection (100%) was calculated from number of plaques, fluorescence, and luciferase values of infected cells in the absence of remdesivir. Means and SD values were calculated from quadruplicates from three independent experiments with Microsoft Excel software. The 50% effective concentration (EC_{50}) was calculated by sigmoidal dose-response curves on GraphPad Prism (San Diego, CA, USA, Version 8.2.1).

Mice experiments

Female 4-6 weeks old K18 hACE2 transgenic mice [B6.Cg-Tg(K18-ACE2)2Prlmn/J, The Jackson laboratory] were maintained in the animal care facility at Texas Biomedical Research Institute under specific pathogen-free conditions. For viral infections, groups of mice were anesthetized with gaseous isoflurane and inoculated intranasally with the indicated viruses. A separate group of K18 hACE2 transgenic mice were also mock-infected with PBS and served as a negative control.

For body weight and survival studies, K18 hACE2 transgenic mice (n=4) were intranasally infected with 10^5 PFUs/mouse of the indicated viruses and monitored daily for body weight loss and survival to access morbidity and mortality, respectively, over a period of 12 days. Mice that were below 75% of their initial body weight were considered to have reached their experimental endpoint and were humanly euthanized.

In vivo bioluminescence imaging of live mice (n=4) was conducted with an Ami HT *in vivo* imaging system (IVIS; Spectral Instruments) at 1, 2, 4, and 6 days post-infection (DPI). At each time points, mice were anesthetized with isoflurane and retro-orbitally injected with 100 µl of Nano-Glo luciferase substrate diluted by 1:10 in PBS. Mice were immediately placed in an isolation chamber and imaged using the Ami HT IVIS. Radiance within the region of interest (ROI) of each mouse was analyzed using the Aura software (Spectral Instruments) and total flux values (protons/s) were normalized to background signal of mock-infected control.

To access fluorescence expression in the lungs and to determine viral titers, a separate cohort of mice (n=4) were similarly infected with the indicated recombinant viruses and were humanely euthanized at 2 and 4 DPI after *in vivo* imaging. Lungs were surgically excised, washed in PBS, and fluorescent and brightfield images were obtained using an Ami HT IVIS and an iPhone 6s (Apple), respectively. Fluorescence signal (radiance efficiency) around the ROI of the lungs were quantified using the Aura software and mean values were normalized to the autofluorescence of mock-infected lungs. The macroscopic pathology score was determined in a blinded manner by a certified pathologist from brightfield images of the lungs, in which the percent of total surface area of lungs affected by consolidation, lesions, congestion, and/or atelectasis was quantified with NIH ImageJ software as previously described (58, 71). Nasal turbinate and brains were also collected, and tissues were individually homogenized in 1 ml of PBS using a Precellys tissue homogenizer (Bertin Instruments). Tissue homogenates were centrifuged at 12,000 x *g* at 4ºC for 5 min to pellet cell debris, and supernatants were collected. Viral titers were determined by plaque assay and immunostaining as described

above. Nluc activity in the tissue homogenates were determined using Nano-Glo luciferase substrate kit and a Synergy LX microplate reader.

Hamster experiments

Female 4-6 weeks old golden Syrian hamsters (*Mesocricetus auratus*) were purchased from Charles River Laboratories and maintained in the animal care facility at Texas Biomedical Research Institute under specific pathogen-free conditions. For viral infections, hamsters were anesthetized with isoflurane and intranasally infected with rSARS-CoV-2/mCherry-Nluc. One day later, infected hamsters were transferred to cages containing contact naïve hamsters. A separate group of hamsters were also mock-infected with PBS and served as a negative control.

In vivo bioluminescence imaging of live hamsters (n=4) was conducted with an Ami HT IVIS on 2, 4 and 6 DPI. Hamsters were anesthetized with gaseous isoflurane in an isolation chamber, and Nano-Glo luciferase substrate was diluted 1:10 in PBS and retro-orbitally injected into each animal (200 µl). Immediately after, hamsters were secured in the isolation chamber and imaged with an Ami HT IVIS and bioluminescence analyses were performed. The total flux values were obtained around the ROI of each hamster and normalized to mock-infected hamsters. Next, hamsters were euthanized, and mCherry expression in excised lungs were imaged in an Ami HT IVIS. The Aura software was used to determine the radiant efficiency of the ROI. Fluorescence signal obtained from infected or contact lungs were normalized to mock-infected lungs. Brightfield images of lungs were taken using an iPhone 6s and were used to assess the pathology score in a blinded manner. A trained pathologist determined the percent of lung surface that was affected by lesions, congestion, consolidation, and/or atelectasis using NIH ImageJ (58, 71). Along

with the lungs, nasal turbinate were excised and homogenized in PBS using a Precellys tissue homogenizer at 12,000 x *g* for 5 min. Supernatants were collected and used to determine viral titers and Nluc activity as described above.

Statistical analysis

All data are presented as mean values and SD for each group and were analyzed using Microsoft Excel software. A one-way ANOVA or student t-test was used for statistical analysis on GraphPad Prism or Microsoft Word software, respectively. *, $p < 0.05$; **, $p < 0.01$; ***, $p < 0.001$; ****, $p < 0.0001$; and ns, no significance.

RESULTS

Generation of rSARS-CoV-2/mCherry-Nluc

Recently, we have generated rSARS-CoV-2 expressing single reporter genes upstream of the viral N gene using a PTV-1 2A autoproteolytic peptide approach (23). These new rSARS-CoV-2 displayed higher levels of reporter gene expression than those previously described in which the reporter gene substitutes the viral ORF7a protein (43-45). To generate a rSARS-CoV-2 expressing two reporter genes, mCherry and Nluc, we implemented a similar method and inserted a fusion sequence of mCherry-Nluc, and the PTV-1 2A autoproteolytic peptide, upstream of the SARS-CoV-2 N gene in the BAC containing a full length copy of the SARS-CoV-2 genome (**Figure 1A**), and rescued rSARS-CoV-2/mCherry-Nluc using our previously described protocol (44, 58). To assess whether mCherry expression could be directly visualized by fluorescence microscopy, Vero E6 cells were mock-infected or infected (MOI 0.01) with rSARS-CoV-2/WT, rSARS-CoV-2/mCherry, rSARS-CoV-2/Nluc, or rSARS-CoV-2/mCherry-Nluc (**Figure 1B**). At 24 hpi, cells were fixed and mCherry expression was directly assessed under a fluorescence microscope, which showed high mCherry fluorescence expression in cells infected with rSARS-CoV-2/mCherry or rSARS-CoV-2/mCherry-Nluc, but not in cells infected with rSARS-CoV-2/WT or rSARS-CoV-2/Nluc (**Figure 1B**). Further, viral infection was detected by indirect immunofluorescence microscopy using an anti-N protein 1C7C7 MAb (**Figure 1B**). As expected, all Vero E6 cells infected with the different rSARS-CoV-2 mutants, but not mock-infected cells, were positive for the presence of the virus. Expression of mCherry and Nluc reporter genes were also confirmed by Western blot (**Figure 1C**). As expected, mCherry was readily detected in whole cell lysates from Vero

E6 cells infected with rSARS-CoV-2/mCherry or rSARS-Cov-2/mCherry-Nluc but not in those infected with rSARS-CoV-2/WT or rSARS-CoV-2/Nluc; or mock-infected (**Figure 1C**). Likewise, Nluc was detected only in cell extracts from rSARS-CoV-2/Nluc and rSARS-CoV-2/mCherry-Nluc infected cells and not in those infected with rSARS-CoV-2/WT or rSARs-CoV-2/mCherry; or mock-infected (**Figure 1C**). A specific band for the viral N protein appeared in all the virus-infected cell extracts, but not in mock-infected Vero E6 cell extracts, all of which showed comparable protein levels of N protein expression (**Figure 1C**). The identity of the double reporter-expressing rSARS-CoV-2/mCherry-Nluc was further validated by next generation sequencing (**Figure 1D).** The rSARS-CoV-2/mCherry and rSARS-CoV-2/Nluc were also sequenced as reference controls. We found two non-reference alleles with a frequency greater than 10% in rSARS-CoV-2/mCherry in the viral N (C752T) and envelope, E (V5A) proteins (**Figure 1D,** top). Likewise, we identified two amino acid changes in the rSARS-CoV-2/Nluc S (H655Y) and E (S6L) proteins (**Figure 1D,** middle). No amino acid changes were found in rSARS-CoV-2/mCherry-Nluc compared to the reference viral genome (**Figure 1D,** bottom), indicating that rSARS-CoV-2/mCherry-Nluc resembles the sequence of rSARS-CoV-2/WT apart from the insertion of the mCherry-Nluc reporter gene fusion and the PTV-1 2A autoproteolytic site.

In vitro **characterization of rSARS-CoV-2/mCherry-Nluc**

Since the cloning of two reporter genes as a fusion protein could affect viral fitness and/or reporter gene expression, we examined the viral fitness of rSARS-CoV-2/mCherry-Nluc in cultured cells by assessing growth kinetics and compared them to those of rSARS-CoV-2 expressing single reporter gene (e.g. rSARS-CoV-2/mCherry and rSARS-CoV-

2/Nluc) or rSARS-CoV-2/WT (**Figure 2A**). Vero E6 cells were infected at an MOI of 0.01 and viral titers in cell culture supernatants were quantified at different time points. No significant difference in replication kinetics were found between all the indicated viruses, except for rSARS-CoV-2/Nluc, which replicated slightly slower (**Figure 2A**). Conversely, rSARS-CoV-2/mCherry-Nluc reached a high titer of 10^7 PFU/ml by 24-48 hpi like rSARS-Co-2/WT and rSARS-CoV-2/mCherry, suggesting that the expression of the double reporter fused mCherry-Nluc gene did not affect viral fitness in Vero E6 cells (**Figure 2A**). In parallel, Nluc and mCherry expression were evaluated over a period of 96 h by either assessing Nluc activity in cell culture supernatants (**Figure 2B**) or by fluorescence microscopy (**Figure 2C**). Vero E6 cells were similarly infected (MOI 0.01) and Nluc activity in cell culture supernatants were quantified at different time points. We found Nluc activity steadily increased beginning at 12 hpi and peaked at 72 hpi, then decreased at 96 hpi (**Figure 2B**). No Nluc activity was detected in cell culture supernatants from mock-infected or Vero E6 cells infected with rSARS-CoV-2/WT or rSARS-CoV-2/mCherry (**Figure 2B**). Similarly, mCherry expression was detected as early as 12 hpi and increased in a time dependent matter until 72 hpi (**Figure 2C**). At 96 hpi, mCherry expression was lightly reduced, which coincided with the decrease in Nluc activity and viral titers at the same time point most likely due to the cytopathic effect (CPE) caused by viral infection. As expected, no mCherry expression was detected in Vero E6 cells infected with rSARS-CoV-2/WT or rSARS-CoV-2/Nluc, or mock-infected (not shown). These results suggest that *in vitro* detection and replication of rSARS-CoV-2/mCherry-Nluc could be monitored and quantified based on the expression of either Nluc (**Figure 2B**) or mCherry (**Figure 2C**) reporter genes.

Next, plaque assays were conducted to further corroborate that all rSARS-CoV-2/mCherry-Nluc viral particles express both mCherry and Nluc reporter genes, and to evaluate plaque phenotype and compared them to that of rSARS-CoV-2 expressing individual reporter genes (rSARS-CoV-2/mCherry and rSARS-CoV-2/Nluc), and rSARS-CoV-2/WT (**Figure 2D**). When plaques were examined by fluorescence microscopy, mCherry-positive plaques were detected in cells infected with rSARS-CoV-2/mCherry and rSARS-CoV-2/mCherry-Nluc (**Figure 2D**). Then, Nluc-positive plaques were detected using an anti-Nluc specific Ab and FITC-conjugated secondary Ab, which only appeared in cells infected with rSARS-CoV-2/Nluc or rSARS-CoV-2/mCherry-Nluc (**Figure 2D**). Importantly, when viral plaques were immunostained with an anti-N protein Ab, they colocalized with mCherry- and/or Nluc-positive plaques (white arrows) in both Vero E6 cells infected with individual reporter-expressing rSARS-CoV-2/mCherry and rSARS-CoV-2/Nluc, as well as in double reporter-expressing rSARS-CoV-2/mCherry-Nluc (**Figure 2D**), demonstrating that all rSARS-CoV-2 plaques contained the reporter gene(s). Although the overall plaque size phenotype did not vary between the different viruses, we did observe smaller plaques produced (amongst the normal sized plaques) in rSARS-CoV-2/mCherry-Nluc experiments (**Figure 2D**).

A double reporter-based neutralization assay for the identification of SARS-CoV-2 neutralizing antibodies and antivirals

To demonstrate the feasibility of implementing our rSARS-CoV-2/mCherry-Nluc to identify and characterize neutralizing Abs (NAbs) and antivirals, we developed a double reporter-based microneutralization assay using 1212C2 hMAb (**Figure 3A**) and remdesivir (**Figure 3B**), which are described and shown to neutralize or inhibit,

460 respectively, SARS-CoV-2 (72, 73). The neutralization activity of 1212C2 was assessed
461 by incubating the hMAb with the indicated rSARS-CoV-2 prior to infection of Vero E6
462 cells, and quantifying Nluc activity in cell culture supernatants (**Figure 3A**, right panel)
463 and mCherry expression (**Figure 3A**, middle panel) using a microplate reader at 24 hpi.
464 As internal control, we conducted the microneutralization assay using immunostaining of
465 rSARS-CoV-2/WT, as previously described (**Figure 3A**, left panel) (69). We determined
466 the 50% neutralization concentration (NT_{50}) of 1212C2 hMAb using sigmoidal dose-
467 response curves. The NT_{50} of 1212C2 hMAb against rSARS-CoV-2/mCherry (2.4 ng) and
468 rSARS-CoV-2/mCherry-Nluc (2.7 ng) as determined by fluorescent mCherry expression
469 were similar to that of rSARS-CoV-2/WT (3 ng) using a classical immunostaining assay,
470 and those reported with the SARS-CoV-2 WA-1 natural isolate (44, 72). Moreover, NT_{50}
471 values of 1212C2 hMAb against rSARS-CoV-2/Nluc or rSARS-CoV-2/mCherry-Nluc
472 determined by Nluc expression (3.0 and 2.0 ng, respectively) were also comparable to
473 those of rSARS-CoV-2/WT (3 ng). To determine whether rSARS-CoV-2/mCherry-Nluc
474 could also be used to assess the effectiveness of antivirals, we quantified the Nluc activity
475 (**Figure 3B**, right panel) and mCherry expression (**Figure 3B**, middle panel) in Vero E6
476 cells infected with the single and double reporter-expressing rSARS-CoV-2 in the
477 presence of serial 3-fold dilutions of remdesivir. As before, we also included rSARS-CoV-
478 2/WT infected cells stained with the MAb against the viral N protein as internal control
479 (**Figure 3B**, left panel). Sigmoidal dose-response curves were developed from reporter
480 expression values and used to calculate the 50% effective concentration (EC_{50}). The
481 EC_{50} values of remdesivir against the indicated viruses were similar to each other,
482 regardless of whether the microneutralization assay used immunostaining (rSARS-CoV-

2/WT, 2 μM; left panel), fluorescence (rSARS-CoV-2/mCherry, 1.7 μM; rSARS-CoV-2/mCherry-Nluc, 1.5 μM; middle panel), or luciferase (rSARS-CoV-2/Nluc, 1.4 μM; rSARS-CoV-2/mCherry-Nluc, 1.5 μM; right panel) (**Figure 3B**). Overall, these results demonstrate the feasibility of using the rSARS-CoV-2 expressing both mCherry and Nluc reporter genes to reliably and quickly evaluate the neutralizing and inhibitory properties of NAbs and/or antivirals, respectively, against SARS-CoV-2 based on mCherry and/or Nluc expression, respectively.

Characterization of rSARS-CoV-2/mCherry-Nluc in K18 hACE2 transgenic mice

Next, we characterized the pathogenicity and ability of rSARS-CoV-2/mCherry-Nluc to replicate in K18 hACE2 transgenic mice using rSARS-CoV-2 expressing individual fluorescent and bioluminescent reporter genes (rSARS-CoV-2/mCherry and rSARS-CoV-2/Nluc, respectively), and rSARS-CoV-2/WT as internal control. One group of mice was infected with a mixture of rSARS-CoV-2/mCherry and rSARS-CoV-2/Nluc. To assess pathogenicity, groups of K18 hACE2 transgenic mice (n=4/group) were mock-infected or infected with 10^5 PFUs of the indicated viruses and changes in body weight (**Figure 4A**) and survival (**Figure 4B**) were monitored for 12 DPI. All mice infected with rSARS-CoV-2 rapidly lost body weight and succumbed to viral infection (**Figures 4A and 4B,** respectively). Most importantly, the virulence of rSARS-CoV-2/mCherry-Nluc was shown to be identical to that of our previously reporter viruses expressing individual mCherry or Nluc (44), or rSARS-CoV-2/WT (69, 74). These data indicate that expression of the fusion of mCherry and Nluc from rSARS-CoV-2/mCherry-Nluc does not result in viral attenuation in K18 hACE2 transgenic mouse model as compared to rSARS-CoV-2/WT.

505 **Tracking viral dynamics of rSARS-CoV-2/mCherry-Nluc infection and pathogenesis**
506 **in K18 hACE2 transgenic mice**

507 Since our rSARS-CoV-2/mCherry-Nluc expresses both fluorescent (mCherry) and
508 luciferase (Nluc) reporter genes, we sought to demonstrate the advantage of using this
509 newly double reporter-expressing rSARS-CoV-2/mCherry-Nluc to track viral replication in
510 live animals. Thus, K18 hACE2 transgenic mice were mock-infected or infected with 10^5
511 PFU of the indicated rSARS-CoV-2 reporter viruses intranasally and Nluc was monitored
512 at 1, 2, 4, and 6 DPI (**Figure 5A**). In mice infected with rSARS-CoV-2/Nluc or rSARS-
513 CoV-2/mCherry-Nluc, or co-infected at the same time with rSARS-CoV-2/Nluc and
514 rSARS-CoV-2/mCherry, we detected Nluc signal as early as 1 DPI, which increased over
515 time (**Figure 5A**). Since IVIS was conducted in the same mouse, viral replication and
516 distribution was followed over time (**Figure 5A**) and bioluminescence intensity around the
517 chest area of the mice was measured in flux (**Figure 5B**). As expected, Nluc expression
518 increased over time until mice succumbed to SARS-CoV-2 infection, consistent with
519 previous literature, including ours (43). Notably, and as expected based on the IVIS
520 (**Figure 5A**), Nluc expression was only readily detected in K18 hACE2 transgenic mice
521 infected with rSARS-CoV-2/Nluc, rSARS-CoV-2/mCherry-Nluc, or co-infected with both,
522 rSARS-CoV-2/mCherry and rSARS-CoV-2/Nluc (**Figure 5B**). No significant differences
523 in flux were observed between the groups of mice infected with the Nluc-expressing
524 rSARS-CoV-2 mutants (**Figure 5B**).

525 As luciferase and fluorescence proteins have different properties and could potentially
526 reveal different readouts as surrogate indicators of viral infection, we next determined and
527 compared Nluc and mCherry expression during infection *in vivo*. Thus, K18 hACE2

transgenic mice (n=4) were mock-infected or infected with rSARS-CoV-2/WT, rSARS-CoV-2/mCherry, rSARS-CoV-2/Nluc, rSARS-CoV-2/mCherry-Nluc, or co-infected with rSARS-CoV-2/mCherry and rSARS-CoV-2/Nluc, then on 2 and 4 DPI, Nluc activity in the entire mouse (**Figures 6A and 6B**) and mCherry expression of whole lungs (**Figures 6C and 6D**) were determined, including the gross pathology score (**Figure 6E**). Like our previous results (**Figure 5**), an increase in Nluc expression from 2 to 4 DPI was observed in K18 hACE2 transgenic mice infected with rSARS-CoV-2/Nluc, rSARS-CoV-2/mCherry-Nluc, or co-infected with rSARS-CoV-2/mCherry and rSARS-CoV-2/Nluc (**Figures 6A**). These results were further confirmed when we determined the flux in the *in vivo* imaged mice (**Figures 6B**). After quantifying Nluc expression, the lungs from mock- and rSARS-CoV-2-infected K18 hACE2 transgenic mice were excised and imaged in the IVIS to determine and quantify mCherry expression (**Figures 6C and 6D,** respectively). We only observed detectable levels of mCherry expression in the lungs of K18 hACE2 transgenic mice infected with rSARS-CoV-2/mCherry, rSARS-coV-2/mCherry-Nluc, or co-infected with both rSARS-CoV-2/mCherry and rSARS-coV-2/Nluc (**Figures 6C and 6D**). Notably, levels of mCherry expression, like those of Nluc were comparable in the lungs of K18 hACE2 transgenic mice infected with the double reporter-expressing rSARS-CoV-2/mCherry-Nluc than those infected with the single rSARS-CoV-2/Nluc, or co-infected with rSARS-CoV-2/mCherry and rSARS-CoV-2/Nluc (**Figures 6C and 6D**). Correlating with *in vivo* and *ex vivo* imaging of the lungs, gross lung pathology scores were comparable in all rSARS-CoV-2-infected K18 hACE2 transgenic mice and more significant at 4 DPI (**Figure 6E**).

Both Nluc activity and viral titers peaked at 2 DPI in the nasal turbinate of mice infected with rSARS-CoV-2/Nluc, rSARS-CoV-2/mCherry-Nluc, or co-infected with rSARS-CoV-2/mCherry and rSARS-CoV-2/Nluc (**Figures 7A and 7B**, left panels) However, in the lungs, Nluc activity remained the same at 2 and 4 DPI, while viral titers decreased at 4 DPI as compared to 2 DPI (**Figures 7A and 7B**, middle panels). Nluc activity in brain homogenates was only evident in the samples from mice infected with rSARS-CoV-2/Nluc, rSARS-CoV-2/mCherry-Nluc, or both rSARS-CoV-2/mCherry and rSARS-CoV-2/Nluc and signals increased in a time dependent matter (**Figure 7A**, right panel). Consistent with previous studies, we were only able to detect SARS-CoV-2 in the brain of two of the four mice infected with rSARS-CoV-2/mCherry-Nluc at 4 DPI (**Figure 7B**, right panel) (43)**.** Altogether, these findings demonstrate the feasibility to asses viral infection *in vivo* in the entire mice by bioluminescence (Nluc), and *ex vivo* in the lungs of infected mice by fluorescence (mCherry) with our double reporter-expressing rSARS-CoV-2/mCherry-Nluc and that the mCherry-Nluc fusion does not have a significant impact in the pathogenesis and replication of the virus in K18 hACE2 transgenic mice, showing similar levels of Nluc or mCherry reporter gene expression than those of rSARS-CoV-2 expressing individual bioluminescence or fluorescence proteins. Notably, viral titers of rSARS-CoV-2 mCherry-Nluc in the nasal turbinate and lungs were comparable to those of a rSARS-CoV-2/WT.

Assessment of SARS-CoV-2 infection and transmission in golden Syrian hamsters

To demonstrate the feasibility of using our double reporter rSARS-CoV-2/mCherry-Nluc to assess viral replication and transmission, golden Syrian hamsters (n=4) were mock-infected or infected with 10^5 PFU/hamster of rSARS-CoV-2/mCherry-Nluc. The day

after infection, non-infected naïve contact hamsters were placed in the same cage with infected hamsters. On 2, 4, and 6 DPI Nluc expression in the entire hamsters were evaluated by IVIS, like in our previous studies using K18 hACE2 transgenic mice. Infected hamsters presented detectable levels of Nluc expression in both the nasal turbinate and lungs at 2 and 4 DPI that decreased at 6 DPI (**Figure 8A**). In contrast, contact hamsters had little to no Nluc signal on 2 DPI that drastically increased on 4 and 6 DPI (**Figure 8A**). The temporal and spatial differences in Nluc signal between originally infected and contact hamsters is most likely due to the route of transmission/infection and the time frame in which the contact hamsters were exposed to the originally infected hamsters. These initial IVIS results were further confirmed by quantification of bioluminescence in hamsters (**Figure 8B**) that showed a decrease in flux in infected hamsters from 2 to 6 DPI and an increase from 2 to 4 DPI and then decreased on 6 DPI in contact hamsters (**Figure 8B**). Subsequently, lungs were excised and imaged in the IVIS for Nluc and mCherry expression (**Figure 8C**). Nluc and mCherry levels of expression correlate between them and with that observed by IVIS in the whole hamster, revealing a time-dependent effect in reporter expression in both infected and contact hamsters that correlate with the levels observed by IVIS (**Figure 8D**). Gross pathology scores in the lungs of infected and contact hamsters were determined from brightfield images with increased scores over time in both infected and contact animals (**Figure 8E**).

Finally, nasal turbinate and lungs from mock and originally infected or contact hamsters were processed to determine Nluc activity (**Figure 9A**) and viral titers (**Figure 9B**). In the nasal turbinate of originally infected hamsters, both Nluc activity and viral titers decreased from 2 to 6 DPI, while in contact hamsters, a time-dependent increase was

observed (**Figures 9A and 9B,** respectively). A similar trend between Nluc signal and viral titers were observed in the lungs of originally infected and contact hamsters. Notably, Nluc signal and viral titers from both groups of infected and contact hamsters correlated with bioluminescence intensity from whole animals and excised lungs (**Figure 8**). Based on these results with rSARS-CoV-2/mCherry-Nluc, viral infection can be monitored in hamsters solely using reporter expression that correlates well with levels of viral replication. Moreover, rSARS-CoV-2 transmission from originally infected to contact hamsters can be easily tracked *in vivo* in the whole animal or *ex vivo* in the lungs (**Figure 8**), and results correlate with those of viral replication (**Figure 9**).

DISCUSSION

Replication-competent, reporter-expressing, recombinant viruses have been previously shown to represent an excellent approach to study, among others, viral infection, replication, pathogenesis, and transmission (19-29). We and others have described the feasibility of generating rSARS-CoV-2 expressing reporter genes encoding either fluorescent or luciferase proteins (36, 43, 44, 46, 47). These reporter-expressing replication-competent rSARS-CoV-2 can be used to assess the prophylactic activity of vaccines and/or the therapeutic potential of NAbs or antivirals (45, 69). Moreover, these rSARS-CoV-2 expressing fluorescent or luciferase proteins represent an excellent option to study the biology of SARS-CoV-2 in cultured cells and/or in validated small animals of infection (44, 45, 47). Moreover, we have described a new approach to express reporter genes from the locus of the viral N protein using a 2A autoproteolytic system where levels of fluorescent or luciferase expression are higher than those where the reporter gene substitutes the viral ORF7a (43, 44). This new 2A strategy to express the reporter gene from the viral N protein locus does not require deleting the viral ORF7a (43, 44). However, these previously described reporter-expressing replication-competent rSARS-CoV-2 only express a single fluorescent or a luciferase protein and, therefore, their experimental applications are limited to the properties of one specific reporter gene and available equipment (43, 44).

Using our previously described BAC-based reverse genetics (19, 57), we generated a rSARS-CoV-2 expressing a fusion of the fluorescent mCherry protein to the bioluminescence Nluc protein (rSARS-CoV-2/mCherry-Nluc) upstream of the viral N protein separated by the PTV-1 2A autoproteolytic cleavage site, thereby allowing

separate expression of the mCherry-Nluc fusion and the viral N protein (43, 44). Expression of both reporter genes was validated by fluorescence microscopy (mCherry) or by luciferase activity with a microplate reader (Nluc). We further confirmed reporter expression by Western blot, where a specific band was detected for the mCherry-Nluc fusion polyprotein. In cell culture, rSARS-CoV-2/mCherry-Nluc displayed growth kinetics similar to those of rSARS-CoV-2 expressing individual mCherry (rSARS-CoV-2/mCherry) or Nluc (rSARS-CoV-2/Nluc), or a rSARS-CoV-2 lacking reporter genes (rSARS-CoV-2/WT). Likewise, the plaque phenotype of the novel rSARS-CoV-2/mCherry-Nluc were similar in size to those of rSARS-CoV-2/mCherry, rSARS-CoV-2/Nluc, or rSARS-CoV-2/WT but only rSARS-CoV-2/mCherry-Nluc had detectable levels of expression of both reporter genes. Importantly, levels of mCherry or Nluc reporter expression correlated with the levels of viral replication, further supporting the concept of reporter genes being a valid surrogate to study viral infection.

Based on the advantages of using a rSARS-CoV-2 expressing both a fluorescent and a bioluminescence protein over those expressing either fluorescence or luciferase reporter genes, we developed a bireporter-based microneutralization assay to identify and characterize NAbs as well as antivirals. Importantly, NT_{50} (NAbs) and EC_{50} (antivirals) values obtained in bireporter-based microneutralization assays using either fluorescence or luciferase signal were comparable to those obtained with rSARS-CoV-2 expressing individual mCherry (rSARS-CoV-2/mCherry) or Nluc (rSARS-CoV-2/Nluc) reporter genes, or rSARS-CoV-2/WT, and those reported previously in the literature (22, 43, 44, 46). Overall, the bireporter rSARS-CoV-2 represents an excellent option in circumstances were fluorescence or luciferase is negated by the properties of an antiviral drug (such as

665 fluorescing chemical entities in certain small molecule compounds) or the host cell being
666 studied (44, 69). Moreover, although in this report the bireporter-based
667 microneutralization assay was performed in 96-well plates, it can be easily adapted to a
668 384-well format for high-throughput screenings (HTS) to identify NAbs or antivirals using
669 a double reporter screening approach based on expression of both fluorescent mCherry
670 and luciferase Nluc. In this instance, having two reporters allows HTS to have the option
671 to use either reporters, or both, to further validate neutralization results.

672 One of the major limitations of recombinant viruses expressing reporter genes is their
673 potential attenuation *in vivo* (37). To assess whether expression of mCherry fused to Nluc
674 affected SARS-CoV-2 replication *in vivo,* we infected K18 hACE2 transgenic mice and
675 golden Syrian hamsters with rSARS-CoV-2/mCherry-Nluc. Despite encoding a fusion of
676 two reporter genes from the locus of the viral N protein, rSARS-CoV-2/mCherry-Nluc
677 displayed similar virulence as determined by changes in body weight and survival in K18
678 hACE2 transgenic mice as rSARS-CoV-2 expressing individual fluorescent (rSARS-CoV-
679 2/mCherry) or luciferase genes (rSARS-CoV-2/Nluc), or rSARS-CoV-2/WT. Importantly
680 we traced viral infection in the same animal over a period of 6 days based on Nluc
681 expression. We were able to detect both luciferase and fluorescent expression in the
682 lungs of mice infected with rSARS-CoV-2/mCherry-Nluc; and mCherry or Nluc expression
683 levels in the lungs of infected mice were comparable to those observed in mice infected
684 with rSARS-CoV-2/mCherry or rSARS-CoV-2/Nluc, or co-infected with both rSARS-CoV-
685 2/mCherry and rSARS-CoV-2/Nluc, or rSARS-CoV-2/WT. Notably, rSARS-CoV-
686 2/mCherry-Nluc replicated in the nasal turbinate, lungs, and brain of infected K18 hACE2
687 transgenic mice to levels comparable to recombinant viruses expressing individual

reporter genes (rSARS-CoV-2/mCherry or rSARS-CoV-2/Nluc) and those of rSARS-CoV-2/WT. Similar results were also observed in the golden Syrian hamster model of SARS-CoV-2 infection and transmission (19, 70). Importantly, in the case of hamsters, we were able to track viral infection and transmission in infected and contact hamsters, respectively, demonstrating the feasibility of using our double reporter-expressing rSARS-CoV-2/mCherry-Nluc in transmission studies in hamsters.

In summary, we have generated a rSARS-CoV-2 expressing simultaneously two reporter genes that is suitable for multiple experimental applications currently not available with the use of rSARS-CoV-2 expressing a single fluorescent or luciferase reporter gene. This rSARS-CoV-2/mCherry-Nluc virus is, to our knowledge, the first replication-competent rSARS-CoV-2 stably expressing two reporter genes. The feasibility of generating rSARS-CoV-2 expressing a fusion of two reporter genes demonstrates the plasticity of the viral genome to express large ORFs from the locus of the viral N protein. Moreover, the robust levels of reporter gene expression obtained using this 2A autoproteolytic approach and the feasibility of expressing foreign genes without the need of removing a viral protein (e.g. ORF7a) represent an ideal option for the use of rSARS-CoV-2/mCherry-Nluc to study viral infection, pathogenesis and transmission, including newly identified VoC.

ACKNOWLEDGEMENTS

We are grateful to Dr. Thomas Moran at The Icahn School of Medicine at Mount Sinai for providing the SARS-CoV cross-reactive 1C7C7 N protein MAb. Research on SARS-CoV-2 in L.M-S laboratory was partially supported by grants W81XWH2110103 and W81XWH2110095 from the Department of Defense (DoD) Peer Reviewed Medical Research Program (PRMRP); 1R43AI165089-01, 1R01AI161363-01 and 1R01AI161175-01A1 from the National Institute of Health (NIH); by the Center for Research on Influenza Pathogenesis (CRIP), one of the National Institute of Allergy and Infectious Diseases (NIAID) funded Centers of Excellence for Influenza Research and Response (CEIRR; contract # 75N93021C00014); the San Antonio Partnership for Precision Therapeutics, and the San Antonio Medical Foundation. Research in L.M-S was also partially supported by NIH R01AI145332, R01AI142985, R01AI141607; and by the DoD W81XWH1910496.

FIGURE LEGENDS

Figure 1. Generation of a bireporter rSARS-CoV-2 expressing mCherry and Nluc (rSARS-CoV-2/mCherry-Nluc). A) Schematic representation of the rSARS-CoV-2/mCherry-Nluc viral genome: SARS-CoV-2 structural, non-structural, and accessory open reading frame (ORF) proteins are indicated in white boxes. mCherry (red), Nluc (blue) and the PTV-1 2A autoproteolytic sequence (black) were inserted in front of the viral N protein. **B) mCherry expression and immunofluorescence assays:** Vero E6 cells (1.2 x 10^6 cells/well, 6-well format, triplicates) were mock-infected or infected (MOI 0.01) with rSARS-CoV-2 WT, rSARS-CoV-2/mCherry, rSARS-CoV-2/Nluc, or rSARS-CoV-2/mCherry-Nluc. Cells were fixed in 10% neutral buffered formalin 24 hpi before directly visualizing mCherry expression under a fluorescence microscope or the viral N protein using a specific 1C7C7 MAb. Cell nuclei were strained with DAPI. Representative images are shown. Scale bars = 100 µm. Magnification = X20. **C) Western blots:** Vero E6 cells (1.2 x 10^6 cells/well, 6-well format, triplicates) were mock-infected or infected (MOI 0.01) with rSARS-CoV-2 WT, rSARS-CoV-2/mCherry, rSARS-CoV-2/Nluc, or rSARS-CoV-2/mCherry-Nluc. At 24 hpi, cells were collected and protein expression in cell lysates were evaluated by Western blot using specific antibodies against SARS-CoV-2 N protein, or the mCherry and Nluc reporter proteins. Tubulin was included as a loading control. The molecular mass of proteins is indicated in kilodaltons (kDa) on the left. **D) Deep sequencing analysis of reporter-expressing rSARS-CoV-2:** The non-reference allele frequency of rSARS-CoV-2/mCherry (top), rSARS-CoV-2/Nluc (middle), and rSARS-CoV-2/mCherry-Nluc (bottom) was calculated by comparing the short reads to the respective reference SARS-CoV-2 WA-1 viral genome (MN985325.1). Non-reference

alleles present in less than 10% of reads are not shown (dotted line) and the non-reference allele frequency that is greater than 10% is indicated.

Figure 2. *In vitro* characterization of the bireporter rSARS-CoV-2/mCherry-Nluc virus. A) Viral growth kinetics: Viral titers (PFU/ml) in the cell culture supernatants of Vero E6 cells (1.2 x 10^6 cells/well, 6-well format, triplicates) infected (MOI 0.01) with rSARS-CoV-2 WT (WT), rSARS-CoV-2/mCherry (mCherry), rSARS-CoV-2/Nluc (Nluc), or rSARS-CoV-2/mCherry-Nluc (mCherry-Nluc) at the indicated time points post-infection were determined by plaque assay. Data represents the mean values and SD of triplicates. LOD, limit of detection. **B) Nluc activity:** Nluc activity in the cell culture supernatants obtained from the experiment in panel A is represented in relative light units (RLU). **C) mCherry expression kinetics:** Vero E6 cells (1.2 x 10^6 cells/well, 6-well format, triplicates) were infected (MOI 0.01) with rSARS-CoV-2 WT, rSARS-CoV-2/mCherry, rSARS-CoV-2/Nluc, or rSARS-CoV-2/mCherry-Nluc and mCherry expression was directly visualized under a fluorescence microscope at the indicated times post-infection. Representative images are shown. Scale bars = 300 μm. Magnification = X10. **D) Plaque phenotype:** Viral plaques from Vero E6 cells (2 x 10^5 cells/well, 24-well plate format, triplicates) infected with rSARS-CoV-2 WT, rSARS-CoV-2/mCherry, rSARS-CoV-2/Nluc, or rSARS-CoV-2/mCherry-Nluc at 3 DPI were observed under a fluorescence imaging system (first column, red filter), fluorescently stained with an antibody against Nluc (second column, FITC), or immunostaining with an antibody against the viral N protein (third column, N). White arrowheads depict the overlapping signal of mCherry fluorescence (left), Nluc bioluminescence (middle), and immunostaining of the viral N

779 protein (right) in Vero E6 cells infected with rSARS-CoV-2/mCherry, rSARS-CoV-2/Nluc,
780 or rSARS-CoV-2/mCherry-Nluc. ns, not significant. *, $P < 0.05$; **, $P < 0.01$.
781 **Figure 3. Bireporter-based microneutralization assay to identify NAbs and**
782 **antivirals against SARS-CoV-2. A) A bireporter microneutralization assay to**
783 **identify NAbs:** Three-fold serial dilutions of the SARS-CoV-2 1212C2 hMAb (starting
784 concentration of 500 ng) were prepared in post-infection media and incubated with 100-
785 200 PFUs/well of rSARS-CoV-2 WT (WT), rSARS-CoV-2/mCherry (mCherry), rSARS-
786 CoV-2/Nluc (Nluc), or rSARS-CoV-2/mCherry-Nluc (mCherry-Nluc) for 1 h at
787 RT. Vero E6 cells (96-well plate format, 4 x 10^4 cells/well, quadruplicates) were infected
788 and incubated with the virus-antibody mixture at 37º C for 24 h. Viral neutralization was
789 determined by immunostaining using an anti-N protein MAb (1C7C7) for rSARS-CoV-
790 2/WT (left) or by fluorescence expression for rSARS-CoV-2/mCherry and rSARS-CoV-
791 2/mCherry-Nluc (middle), or bioluminescence for rSARS-CoV-2/Nluc and rSARS-CoV-
792 2/mCherry-Nluc (right) using a microplate reader. The 50% neutralization titer (NT_{50}) was
793 calculated using sigmoidal dose-response curves on GraphPad Prism. Viral
794 neutralization was normalized to wells containing infected cells without the 1212C2 hMAb.
795 The dotted line indicates 50% virus inhibition. Data are represented by the mean values
796 and SD of quadruplicates. **B) A bireporter microneutralization assay to assess**
797 **antivirals:** Vero E6 cells (96-well plate format, 4 x 10^4 cells/well, quadruplicates) were
798 infected with 100-200 PFUs of rSARS-CoV-2/WT, or reporter viruses expressing
799 mCherry, Nluc, or mCherry-Nluc. After 1 h viral absorption, cells were incubated in post-
800 infection media containing 3-fold serial dilutions of remdesivir (starting concentration of
801 100 µM). Viral inhibition was determined by immunostaining using an anti-N protein MAb

(1C7C7) for rSARS-CoV-2/WT (left) or by fluorescence expression for rSARS-CoV-2/mCherry and rSARS-CoV-2/mCherry-Nluc (middle), or bioluminescence for rSARS-CoV-2/Nluc and rSARS-CoV-2/mCherry-Nluc (right) using a microplate reader. The 50% effective concentration (EC_{50}) was calculated using sigmoidal dose-response curves on GraphPad Prism. Viral inhibition was normalized to wells containing infected cells without remdesivir. The dotted line indicates the 50% virus inhibition. The data is represented by the mean values and SD of quadruplicates.

Figure 4. Virulence of rSARS-CoV-2/mCherry-Nluc in K18 hACE2 transgenic mice: Four-to-six-weeks-old female K18 hACE2 transgenic mice (n=4) were mock-infected or intranasally inoculated with 10^5 PFU/mouse of rSARS-CoV-2 WT (WT), rSARS-CoV-2/mCherry (mCherry), rSARS-CoV-2/Nluc (Nluc), or the bireporter rSARS-CoV-2/mCherry-Nluc (mCherry-Nluc). A group of four-to-six-weeks-old female K18 hACE2 transgenic mice (n=4) were also co-infected with rSARS-CoV-2/mCherry and rSARS-CoV-2/Nluc (mCherry + Nluc). Body weight loss (**A**) and survival (**B**) of mice were monitored for 12 days after viral infection.

Figure 5. *In vivo* kinetics of rSARS-CoV-2/mCherry-Nluc in K18 hACE2 transgenic mice: Four-to-six-weeks-old female K18 hACE2 transgenic mice (n=4) were mock-infected or infected intranasally with 10^5 PFU/mouse of rSARS-CoV-2 WT, rSARS-CoV-2/mCherry, rSARS-CoV-2/Nluc, rSARS-CoV-2/mCherry + rSARS-CoV-2/Nluc, or with rSARS-CoV-2/mCherry-Nluc (mCherry-Nluc). Nluc activity in the whole mouse at the indicated DPI was evaluated with an Ami HT *in vivo* imaging system. Representative images of the same mouse at 1, 2, 4, and 6 DPI are shown (**A**). Means and SD of the radiance (number of photons per second per square centimeter per steradian

825 [p/second/cm2/sr]) and bioluminescence (total flux [log_{10} photons per second (p/s)] over
826 each mouse are shown) (**B**). ns, not significant. ***, $P < 0.001$.

827 **Figure 6. *In vivo* bioluminescence and *ex vivo* fluorescence in K18 hACE2**
828 **transgenic mice infected with rSARS-CoV-2/mCherry-Nluc. A) *In vivo* Nluc**
829 **expression:** Nluc activity in live mice (n=4) mock-infected or infected (10^5 PFU/mouse)
830 with rSARS-CoV-2 WT, rSARS-CoV-2/mCherry, rSARS-CoV-2/Nluc, rSARS-CoV-
831 2/mCherry + rSARS-CoV-2/Nluc, or the bireporter rSARS-CoV-2/mCherry-Nluc
832 (mCherry-Nluc) were determined on 2 and 4 DPI using the Ami HT IVIS. A representative
833 image of a mouse per time point is shown. **B) Quantification of Nluc signal:** Means and
834 SD of the radiance (number of photons per second per square centimeter per steradian
835 [p/second/cm2/sr]) and bioluminescence (total flux [log_{10} photons per second (p/s)] of
836 mock and infected mice is shown. **C) *Ex vivo* mCherry expression:** Excised lungs from
837 mock-infected or infected mice from panel A were monitored for mCherry fluorescent
838 expression (FL, top) and bright field (BF, bottom) at 2 and 4 DPI. Representative lung
839 images from the same mouse used in panel A are shown. **D) Quantification of mCherry**
840 **expression:** The mean values of mCherry signal around the regions of interest were
841 normalized to the autofluorescence of mock-infected lungs at each time point and the fold
842 changes in fluorescence were calculated. **E) Gross pathology score:** Pathology lesions,
843 consolidation, congestion, and atelectasis, of excised lungs were measured using NIH
844 ImageJ and represented as percentages of total lung surface area affected. ns, not
845 significant. *, $P < 0.05$; ***, $P < 0.001$.

846 **Figure 7. Nluc activity and viral titers in tissue homogenates from infected K18**
847 **hACE2 transgenic mice:** The nasal turbinate (left), lungs (middle), and brain (right) of

four-to-six-weeks-old female K18 hACE2 transgenic mice (n=4) mock-infected or infected intranasally with 10^5 PFU/mouse of rSARS-CoV-2 WT, rSARS-CoV-2/mCherry, rSARS-CoV-2/Nluc, rSARS-CoV-2/mCherry + rSARS-CoV-2/Nluc, or the bireporter rSARS-CoV-2/mCherry-Nluc were collected after imaging on an Ami HT IVIS on 2 and 4 DPI. After homogenization, Nluc activity (**A**) and viral titers (**B**) in tissue homogenates were determined on a microplate reader or by plaque assay, respectively. The results are the mean values and SD. LOD, limit of detection. ns, not significant. nd, not detected. **, $P < 0.01$; ***, $P < 0.001$.

Figure 8. *In vivo* bioluminescence and *ex vivo* fluorescence in golden Syrian hamsters infected with rSARS-CoV-2/mCherry-Nluc. A) *In vivo* Nluc expression: Nluc activity in four-to-six-weeks-old female golden Syrian hamsters (n=4) mock-infected or infected with 10^5 PFU/hamster of rSARS-CoV-2/mCherry-Nluc were determined on 2, 4 and 6 DPI using the Ami HT IVIS. Contact animals were exposed to infected animals 1 DPI. A representative image of a hamster per time points and experimental condition is shown. **B) Quantification of Nluc signal:** Means and SD of the radiance (number of photons per second per square centimeter per steradian [p/second/cm2/sr]) and bioluminescence (total flux [$\log_{10}$ photons per second (p/s)] were quantified from whole hamsters after IVIS imaging. **C) *Ex vivo* mCherry and Nluc expression:** Excised lungs from mock-infected or infected golden Syrian hamsters from panel A were monitored for mCherry fluorescence (FL, top), Nluc signal (Nluc, middle), and bright field (BF, bottom) at 2, 4, and 6 DPI. Representative lung images from the same hamster used in panel A are shown. **D) Quantification of mCherry expression:** the mean values of mCherry signal around the regions of interest were normalized to the autofluorescence of mock-

infected lungs at each time point and the fold changes in fluorescence were calculated. **E) Gross pathology score:** Pathological lesions, consolidation, congestion, and atelectasis, of excised lungs were measured using NIH ImageJ and represented as percentages of total lung surface area affected. ns, not significant. *, $P < 0.05$; ***, $P < 0.001$.

Figure 9. Nluc activity and viral titers in golden Syrian hamster tissue homogenates infected with rSARS-CoV-2/mCherry-Nluc: The nasal turbinate (left) and lungs (right) of four-to-six-weeks-old female golden Syrian hamsters (n=4) mock-infected or infected intranasally with 10^5 PFU/hamster of rSARS-CoV-2/mCherry-Nluc were collected after imaging on an Ami HT IVIS at 2 and 4 DPI. In addition, after 24 hpi, contact golden Syrian hamsters (n=4, contact) were added to the cages of infected animals. After homogenization, Nluc activity (**A**) and viral titers (**B**) in tissue homogenates were determined on a microplate reader or by plaque assay, respectively. Results are the means and SD. LOD, limit of detection. ns, not significant. nd, not detected. ***, $P < 0.001$.

REFERENCES

1. Zhu N, Zhang D, Wang W, Li X, Yang B, Song J, Zhao X, Huang B, Shi W, Lu R, Niu P, Zhan F, Ma X, Wang D, Xu W, Wu G, Gao GF, Tan W, China Novel Coronavirus I, Research T. 2020. A Novel Coronavirus from Patients with Pneumonia in China, 2019. N Engl J Med 382:727-733.
2. Dong E, Du H, Gardner L. 2020. An interactive web-based dashboard to track COVID-19 in real time. Lancet Infect Dis 20:533-534.
3. Mizumoto K, Kagaya K, Zarebski A, Chowell G. 2020. Estimating the asymptomatic proportion of coronavirus disease 2019 (COVID-19) cases on board the Diamond Princess cruise ship, Yokohama, Japan, 2020. Euro Surveill 25.
4. Gudbjartsson DF, Helgason A, Jonsson H, Magnusson OT, Melsted P, Norddahl GL, Saemundsdottir J, Sigurdsson A, Sulem P, Agustsdottir AB, Eiriksdottir B, Fridriksdottir R, Gardarsdottir EE, Georgsson G, Gretarsdottir OS, Gudmundsson KR, Gunnarsdottir TR, Gylfason A, Holm H, Jensson BO, Jonasdottir A, Jonsson F, Josefsdottir KS, Kristjansson T, Magnusdottir DN, le Roux L, Sigmundsdottir G, Sveinbjornsson G, Sveinsdottir KE, Sveinsdottir M, Thorarensen EA, Thorbjornsson B, Löve A, Masson G, Jonsdottir I, Möller AD, Gudnason T, Kristinsson KG, Thorsteinsdottir U, Stefansson K. 2020. Spread of SARS-CoV-2 in the Icelandic Population. N Engl J Med 382:2302-2315.
5. Zaki AM, van Boheemen S, Bestebroer TM, Osterhaus AD, Fouchier RA. 2012. Isolation of a novel coronavirus from a man with pneumonia in Saudi Arabia. N Engl J Med 367:1814-20.

916 6. de Wit E, van Doremalen N, Falzarano D, Munster VJ. 2016. SARS and MERS:
917 recent insights into emerging coronaviruses. Nat Rev Microbiol 14:523-34.
918 7. Chen B, Tian EK, He B, Tian L, Han R, Wang S, Xiang Q, Zhang S, El Arnaout T,
919 Cheng W. 2020. Overview of lethal human coronaviruses. Signal Transduct Target
920 Ther 5:89.
921 8. Kahn JS. 2006. The widening scope of coronaviruses. Curr Opin Pediatr 18:42-7.
922 9. Peacock TP, Goldhill DH, Zhou J, Baillon L, Frise R, Swann OC, Kugathasan R,
923 Penn R, Brown JC, Sanchez-David RY, Braga L, Williamson MK, Hassard JA,
924 Staller E, Hanley B, Osborn M, Giacca M, Davidson AD, Matthews DA, Barclay
925 WS. 2021. The furin cleavage site in the SARS-CoV-2 spike protein is required for
926 transmission in ferrets. Nat Microbiol 6:899-909.
927 10. Johnson BA, Xie X, Bailey AL, Kalveram B, Lokugamage KG, Muruato A, Zou J,
928 Zhang X, Juelich T, Smith JK, Zhang L, Bopp N, Schindewolf C, Vu M,
929 Vanderheiden A, Winkler ES, Swetnam D, Plante JA, Aguilar P, Plante KS, Popov
930 V, Lee B, Weaver SC, Suthar MS, Routh AL, Ren P, Ku Z, An Z, Debbink K,
931 Diamond MS, Shi PY, Freiberg AN, Menachery VD. 2021. Loss of furin cleavage
932 site attenuates SARS-CoV-2 pathogenesis. Nature 591:293-299.
933 11. Wang M, Cao R, Zhang L, Yang X, Liu J, Xu M, Shi Z, Hu Z, Zhong W, Xiao G.
934 2020. Remdesivir and chloroquine effectively inhibit the recently emerged novel
935 coronavirus (2019-nCoV) in vitro. Cell Res 30:269-271.
936 12. Beigel JH, Tomashek KM, Dodd LE, Mehta AK, Zingman BS, Kalil AC, Hohmann
937 E, Chu HY, Luetkemeyer A, Kline S, Lopez de Castilla D, Finberg RW, Dierberg
938 K, Tapson V, Hsieh L, Patterson TF, Paredes R, Sweeney DA, Short WR,

939 Touloumi G, Lye DC, Ohmagari N, Oh MD, Ruiz-Palacios GM, Benfield T,
940 Fatkenheuer G, Kortepeter MG, Atmar RL, Creech CB, Lundgren J, Babiker AG,
941 Pett S, Neaton JD, Burgess TH, Bonnett T, Green M, Makowski M, Osinusi A,
942 Nayak S, Lane HC, Members A-SG. 2020. Remdesivir for the Treatment of Covid-
943 19 - Final Report. N Engl J Med 383:1813-1826.
944 13. Jones BE, Brown-Augsburger PL, Corbett KS, Westendorf K, Davies J, Cujec TP,
945 Wiethoff CM, Blackbourne JL, Heinz BA, Foster D, Higgs RE, Balasubramaniam
946 D, Wang L, Zhang Y, Yang ES, Bidshahri R, Kraft L, Hwang Y, Žentelis S, Jepson
947 KR, Goya R, Smith MA, Collins DW, Hinshaw SJ, Tycho SA, Pellacani D, Xiang P,
948 Muthuraman K, Sobhanifar S, Piper MH, Triana FJ, Hendle J, Pustilnik A, Adams
949 AC, Berens SJ, Baric RS, Martinez DR, Cross RW, Geisbert TW, Borisevich V,
950 Abiona O, Belli HM, de Vries M, Mohamed A, Dittmann M, Samanovic MI, Mulligan
951 MJ, Goldsmith JA, Hsieh CL, Johnson NV, et al. 2021. The neutralizing antibody,
952 LY-CoV555, protects against SARS-CoV-2 infection in nonhuman primates. Sci
953 Transl Med 13.
954 14. Madhi SA, Baillie V, Cutland CL, Voysey M, Koen AL, Fairlie L, Padayachee SD,
955 Dheda K, Barnabas SL, Bhorat QE, Briner C, Kwatra G, Ahmed K, Aley P, Bhikha
956 S, Bhiman JN, Bhorat AE, du Plessis J, Esmail A, Groenewald M, Horne E, Hwa
957 SH, Jose A, Lambe T, Laubscher M, Malahleha M, Masenya M, Masilela M,
958 McKenzie S, Molapo K, Moultrie A, Oelofse S, Patel F, Pillay S, Rhead S, Rodel
959 H, Rossouw L, Taoushanis C, Tegally H, Thombrayil A, van Eck S, Wibmer CK,
960 Durham NM, Kelly EJ, Villafana TL, Gilbert S, Pollard AJ, de Oliveira T, Moore PL,

961 Sigal A, et al. 2021. Efficacy of the ChAdOx1 nCoV-19 Covid-19 Vaccine against
962 the B.1.351 Variant. N Engl J Med 384:1885-1898.
963 15. Irfan N, Chagla Z. 2021. In South Africa, a 2-dose Oxford/AZ vaccine did not
964 prevent mild to moderate COVID-19 (cases mainly B.1.351 variant). Ann Intern
965 Med 174:JC50.
966 16. Tegally H, Wilkinson E, Giovanetti M, Iranzadeh A, Fonseca V, Giandhari J,
967 Doolabh D, Pillay S, San EJ, Msomi N, Mlisana K, von Gottberg A, Walaza S,
968 Allam M, Ismail A, Mohale T, Glass AJ, Engelbrecht S, Van Zyl G, Preiser W,
969 Petruccione F, Sigal A, Hardie D, Marais G, Hsiao M, Korsman S, Davies M-A,
970 Tyers L, Mudau I, York D, Maslo C, Goedhals D, Abrahams S, Laguda-Akingba O,
971 Alisoltani-Dehkordi A, Godzik A, Wibmer CK, Sewell BT, Lourenço J, Alcantara
972 LCJ, Pond SLK, Weaver S, Martin D, Lessells RJ, Bhiman JN, Williamson C, de
973 Oliveira T. 2020. Emergence and rapid spread of a new severe acute respiratory
974 syndrome-related coronavirus 2 (SARS-CoV-2) lineage with multiple spike
975 mutations in South Africa. medRxiv
976 doi:10.1101/2020.12.21.20248640:2020.12.21.20248640.
977 17. Andrews N, Stowe J, Kirsebom F, Toffa S, Rickeard T, Gallagher E, Gower C, Kall
978 M, Groves N, O'Connell AM, Simons D, Blomquist PB, Zaidi A, Nash S, Iwani Binti
979 Abdul Aziz N, Thelwall S, Dabrera G, Myers R, Amirthalingam G, Gharbia S,
980 Barrett JC, Elson R, Ladhani SN, Ferguson N, Zambon M, Campbell CNJ, Brown
981 K, Hopkins S, Chand M, Ramsay M, Lopez Bernal J. 2022. Covid-19 Vaccine
982 Effectiveness against the Omicron (B.1.1.529) Variant. N Engl J Med
983 doi:10.1056/NEJMoa2119451.

18. Chenchula S, Karunakaran P, Sharma S, Chavan M. 2022. Current evidence on efficacy of COVID-19 booster dose vaccination against the Omicron variant: A systematic review. J Med Virol doi:10.1002/jmv.27697.

19. Ye C, Chiem K, Park JG, Oladunni F, Platt RN, Anderson T, Almazan F, de la Torre JC, Martinez-Sobrido L. 2020. Rescue of SARS-CoV-2 from a single bacterial artificial chromosome. bioRxiv doi:10.1101/2020.07.22.216358.

20. Avila-Perez G, Nogales A, Park JG, Vasquez DM, Dean DA, Barravecchia M, Perez DR, Almazan F, Martinez-Sobrido L. 2020. In vivo rescue of recombinant Zika virus from an infectious cDNA clone and its implications in vaccine development. Sci Rep 10:512.

21. Avila-Perez G, Park JG, Nogales A, Almazan F, Martinez-Sobrido L. 2019. Rescue of Recombinant Zika Virus from a Bacterial Artificial Chromosome cDNA Clone. J Vis Exp doi:10.3791/59537.

22. Xie X, Muruato A, Lokugamage KG, Narayanan K, Zhang X, Zou J, Liu J, Schindewolf C, Bopp NE, Aguilar PV, Plante KS, Weaver SC, Makino S, LeDuc JW, Menachery VD, Shi PY. 2020. An Infectious cDNA Clone of SARS-CoV-2. Cell Host Microbe 27:841-848 e3.

23. Caì Y, Iwasaki M, Beitzel BF, Yú S, Postnikova EN, Cubitt B, DeWald LE, Radoshitzky SR, Bollinger L, Jahrling PB, Palacios GF, de la Torre JC, Kuhn JH. 2018. Recombinant Lassa Virus Expressing Green Fluorescent Protein as a Tool for High-Throughput Drug Screens and Neutralizing Antibody Assays. Viruses 10.

24. Nogales A, Perez DR, Santos J, Finch C, Martinez-Sobrido L. 2017. Reverse Genetics of Influenza B Viruses. Methods Mol Biol 1602:205-238.

1007 25. Breen M, Nogales A, Baker SF, Martínez-Sobrido L. 2016. Replication-Competent
1008 Influenza A Viruses Expressing Reporter Genes. Viruses 8.
1009 26. Engelhardt OG. 2013. Many ways to make an influenza virus--review of influenza
1010 virus reverse genetics methods. Influenza Other Respir Viruses 7:249-56.
1011 27. Ujike M, Etoh Y, Urushiyama N, Taguchi F, Asanuma H, Enjuanes L, Kamitani W.
1012 2022. Reverse Genetics with a Full-Length Infectious cDNA Clone of Bovine
1013 Torovirus. J Virol 96:e0156121.
1014 28. Amarilla AA, Sng JDJ, Parry R, Deerain JM, Potter JR, Setoh YX, Rawle DJ, Le
1015 TT, Modhiran N, Wang X, Peng NYG, Torres FJ, Pyke A, Harrison JJ, Freney ME,
1016 Liang B, McMillan CLD, Cheung STM, Guevara DJDC, Hardy JM, Bettington M,
1017 Muller DA, Coulibaly F, Moore F, Hall RA, Young PR, Mackenzie JM, Hobson-
1018 Peters J, Suhrbier A, Watterson D, Khromykh AA. 2021. A versatile reverse
1019 genetics platform for SARS-CoV-2 and other positive-strand RNA viruses. Nat
1020 Commun 12:3431.
1021 29. Feng M, Li L, Cheng R, Yuan Y, Dong Y, Chen M, Guo R, Yao M, Xu Y, Zhou Y,
1022 Wu J, Ding XS, Zhou X, Tao X. 2021. Development of a Mini-Replicon-Based
1023 Reverse-Genetics System for Rice Stripe Tenuivirus. J Virol 95:e0058921.
1024 30. Smith A, Rodriguez L, Ghouayel ME, Nogales A, Chamberlain JM, Sortino K, Reilly
1025 E, Feng C, Topham DJ, Martinez-Sobrido L, Dewhurst S. 2019. A live-attenuated
1026 influenza vaccine (LAIV) elicits enhanced heterologous protection when the
1027 internal genes of the vaccine are matched to the challenge virus. J Virol
1028 doi:JVI.01065-19 [pii]
1029 10.1128/JVI.01065-19.

1030 31. Rodriguez L, Blanco-Lobo P, Reilly EC, Maehigashi T, Nogales A, Smith A,
1031 Topham DJ, Dewhurst S, Kim B, Martinez-Sobrido L. 2019. Comparative Study of
1032 the Temperature Sensitive, Cold Adapted and Attenuated Mutations Present in the
1033 Master Donor Viruses of the Two Commercial Human Live Attenuated Influenza
1034 Vaccines. Viruses 11.
1035 32. Blanco-Lobo P, Rodriguez L, Reedy S, Oladunni FS, Nogales A, Murcia PR,
1036 Chambers TM, Martinez-Sobrido L. 2019. A Bivalent Live-Attenuated Vaccine for
1037 the Prevention of Equine Influenza Virus. Viruses 11.
1038 33. Rodriguez L, Reedy S, Nogales A, Murcia PR, Chambers TM, Martinez-Sobrido L.
1039 2018. Development of a novel equine influenza virus live-attenuated vaccine.
1040 Virology 516:76-85.
1041 34. Jack BR, Boutz DR, Paff ML, Smith BL, Bull JJ, Wilke CO. 2017. Reduced Protein
1042 Expression in a Virus Attenuated by Codon Deoptimization. G3 (Bethesda) 7:2957-
1043 2968.
1044 35. Fan RL, Valkenburg SA, Wong CK, Li OT, Nicholls JM, Rabadan R, Peiris JS,
1045 Poon LL. 2015. Generation of Live Attenuated Influenza Virus by Using Codon
1046 Usage Bias. J Virol 89:10762-73.
1047 36. Chiem K, Lorenzo M, Rangel-Moreno J, De La Luz Garcia-Hernandez M, Park J-
1048 G, Nogales A, Blasco R, Martínez-Sobrido L. 2021. Bi-reporter vaccinia virus for
1049 tracking viral infections in vitro and in vivo. bioRxiv
1050 doi:10.1101/2021.08.24.457594:2021.08.24.457594.

1051 37. Nogales A, Ávila-Pérez G, Rangel-Moreno J, Chiem K, DeDiego ML, Martínez-
1052 Sobrido L. 2019. A novel fluorescent and bioluminescent Bi-Reporter influenza A
1053 virus (BIRFLU) to evaluate viral infections. J Virol doi:10.1128/JVI.00032-19.
1054 38. DiPiazza A, Nogales A, Poulton N, Wilson PC, Martinez-Sobrido L, Sant AJ. 2017.
1055 Pandemic 2009 H1N1 Influenza Venus reporter virus reveals broad diversity of
1056 MHC class II-positive antigen-bearing cells following infection in vivo. Scientific
1057 Reports 7:10857.
1058 39. Zou G, Xu HY, Qing M, Wang QY, Shi PY. 2011. Development and
1059 characterization of a stable luciferase dengue virus for high-throughput screening.
1060 Antiviral Res 91:11-9.
1061 40. Ozawa M, Victor ST, Taft AS, Yamada S, Li C, Hatta M, Das SC, Takashita E,
1062 Kakugawa S, Maher EA, Neumann G, Kawaoka Y. 2011. Replication-incompetent
1063 influenza A viruses that stably express a foreign gene. J Gen Virol 92:2879-88.
1064 41. Rimmelzwaan GF, Verburgh RJ, Nieuwkoop NJ, Bestebroer TM, Fouchier RA,
1065 Osterhaus AD. 2011. Use of GFP-expressing influenza viruses for the detection of
1066 influenza virus A/H5N1 neutralizing antibodies. Vaccine 29:3424-30.
1067 42. Nogales A, Baker SF, Martínez-Sobrido L. 2015. Replication-competent influenza
1068 A viruses expressing a red fluorescent protein. Virology 476:206-16.
1069 43. Ye C, Chiem K, Park J-G, Silvas JA, Vasquez DM, Torrelles JB, Kobie JJ, Walter
1070 MR, de la Torre JC, Martinez-Sobrido L. 2021. Visualization of SARS-CoV-2
1071 infection dynamic. bioRxiv doi:10.1101/2021.06.03.446942:2021.06.03.446942.
1072 44. Chiem K, Morales Vasquez D, Park JG, Platt RN, Anderson T, Walter MR, Kobie
1073 JJ, Ye C, Martinez-Sobrido L. 2021. Generation and Characterization of

recombinant SARS-CoV-2 expressing reporter genes. J Virol doi:10.1128/JVI.02209-20.

45. Chiem K, Morales Vasquez D, Silvas JA, Park JG, Piepenbrink MS, Sourimant J, Lin MJ, Greninger AL, Plemper RK, Torrelles JB, Walter MR, de la Torre JC, Kobie JK, Ye C, Martinez-Sobrido L. 2021. A Bifluorescent-Based Assay for the Identification of Neutralizing Antibodies against SARS-CoV-2 Variants of Concern. J Virol 95:e0112621.

46. Xie X, Muruato AE, Zhang X, Lokugamage KG, Fontes-Garfias CR, Zou J, Liu J, Ren P, Balakrishnan M, Cihlar T, Tseng C-TK, Makino S, Menachery VD, Bilello JP, Shi P-Y. 2020. A nanoluciferase SARS-CoV-2 for rapid neutralization testing and screening of anti-infective drugs for COVID-19. bioRxiv doi:10.1101/2020.06.22.165712:2020.06.22.165712.

47. Xie X, Muruato A, Lokugamage KG, Narayanan K, Zhang X, Zou J, Liu J, Schindewolf C, Bopp NE, Aguilar PV, Plante KS, Weaver SC, Makino S, LeDuc JW, Menachery VD, Shi PY. 2020. An Infectious cDNA Clone of SARS-CoV-2. Cell Host Microbe 27:841-848.e3.

48. Hall MP, Unch J, Binkowski BF, Valley MP, Butler BL, Wood MG, Otto P, Zimmerman K, Vidugiris G, Machleidt T, Robers MB, Benink HA, Eggers CT, Slater MR, Meisenheimer PL, Klaubert DH, Fan F, Encell LP, Wood KV. 2012. Engineered luciferase reporter from a deep sea shrimp utilizing a novel imidazopyrazinone substrate. ACS Chem Biol 7:1848-57.

1095 49. Tam JM, Upadhyay R, Pittet MJ, Weissleder R, Mahmood U. 2007. Improved in
1096 vivo whole-animal detection limits of green fluorescent protein-expressing tumor
1097 lines by spectral fluorescence imaging. Mol Imaging 6:269-76.
1098 50. Zhao H, Doyle TC, Coquoz O, Kalish F, Rice BW, Contag CH. 2005. Emission
1099 spectra of bioluminescent reporters and interaction with mammalian tissue
1100 determine the sensitivity of detection in vivo. Journal of Biomedical Optics
1101 10:41210.
1102 51. Vintersten K, Monetti C, Gertsenstein M, Zhang P, Laszlo L, Biechele S, Nagy A.
1103 2004. Mouse in red: red fluorescent protein expression in mouse ES cells,
1104 embryos, and adult animals. Genesis 40:241-6.
1105 52. Kelkar M, De A. 2012. Bioluminescence based in vivo screening technologies. Curr
1106 Opin Pharmacol 12:592-600.
1107 53. Shaner NC, Patterson GH, Davidson MW. 2007. Advances in fluorescent protein
1108 technology. J Cell Sci 120:4247-60.
1109 54. Welsh DK, Noguchi T. 2012. Cellular bioluminescence imaging. Cold Spring
1110 Harbor Protocols 2012.
1111 55. Nogales A, Rodriguez-Sanchez I, Monte K, Lenschow DJ, Perez DR, Martinez-
1112 Sobrido L. 2016. Replication-competent fluorescent-expressing influenza B virus.
1113 Virus Res 213:69-81.
1114 56. Chiem K, Rangel-Moreno J, Nogales A, Martinez-Sobrido L. 2019. A Luciferase-
1115 fluorescent Reporter Influenza Virus for Live Imaging and Quantification of Viral
1116 Infection. J Vis Exp doi:10.3791/59890.

1117 57. Chiem K, Ye C, Martinez-Sobrido L. 2020. Generation of Recombinant SARS-
1118 CoV-2 Using a Bacterial Artificial Chromosome. Curr Protoc Microbiol 59:e126.
1119 58. Ye C, Chiem K, Park JG, Oladunni F, Platt RN, 2nd, Anderson T, Almazan F, de
1120 la Torre JC, Martinez-Sobrido L. 2020. Rescue of SARS-CoV-2 from a Single
1121 Bacterial Artificial Chromosome. mBio 11.
1122 59. Almazán F, Dediego ML, Galán C, Escors D, Alvarez E, Ortego J, Sola I, Zuñiga
1123 S, Alonso S, Moreno JL, Nogales A, Capiscol C, Enjuanes L. 2006. Construction
1124 of a severe acute respiratory syndrome coronavirus infectious cDNA clone and a
1125 replicon to study coronavirus RNA synthesis. J Virol 80:10900-6.
1126 60. Bindels DS, Haarbosch L, van Weeren L, Postma M, Wiese KE, Mastop M,
1127 Aumonier S, Gotthard G, Royant A, Hink MA, Gadella TW. 2017. mScarlet: a bright
1128 monomeric red fluorescent protein for cellular imaging. Nat Methods 14:53-56.
1129 61. Luker KE, Pata P, Shemiakina II, Pereverzeva A, Stacer AC, Shcherbo DS,
1130 Pletnev VZ, Skolnaja M, Lukyanov KA, Luker GD, Pata I, Chudakov DM. 2015.
1131 Comparative study reveals better far-red fluorescent protein for whole body
1132 imaging. Sci Rep 5:10332.
1133 62. Shcherbo D, Merzlyak EM, Chepurnykh TV, Fradkov AF, Ermakova GV, Solovieva
1134 EA, Lukyanov KA, Bogdanova EA, Zaraisky AG, Lukyanov S, Chudakov DM.
1135 2007. Bright far-red fluorescent protein for whole-body imaging. Nat Methods
1136 4:741-6.
1137 63. Stacer AC, Nyati S, Moudgil P, Iyengar R, Luker KE, Rehemtulla A, Luker GD.
1138 2013. NanoLuc reporter for dual luciferase imaging in living animals. Mol Imaging
1139 12:1-13.

64. Sewe SO, Silva G, Sicat P, Seal SE, Visendi P. 2022. Trimming and Validation of Illumina Short Reads Using Trimmomatic, Trinity Assembly, and Assessment of RNA-Seq Data. Methods Mol Biol 2443:211-232.

65. Bolger AM, Lohse M, Usadel B. 2014. Trimmomatic: a flexible trimmer for Illumina sequence data. Bioinformatics 30:2114-20.

66. Langmead B, Salzberg SL. 2012. Fast gapped-read alignment with Bowtie 2. Nat Methods 9:357-9.

67. Pedersen BS, Quinlan AR. 2018. Mosdepth: quick coverage calculation for genomes and exomes. Bioinformatics 34:867-868.

68. Wilm A, Aw PP, Bertrand D, Yeo GH, Ong SH, Wong CH, Khor CC, Petric R, Hibberd ML, Nagarajan N. 2012. LoFreq: a sequence-quality aware, ultra-sensitive variant caller for uncovering cell-population heterogeneity from high-throughput sequencing datasets. Nucleic Acids Res 40:11189-201.

69. Park J-G, Oladunni FS, Chiem K, Ye C, Pipenbrink M, Moran T, Walter MR, Kobie J, Martinez-Sobrido L. 2021. Rapid in vitro assays for screening neutralizing antibodies and antivirals against SARS-CoV-2. Journal of Virological Methods 287:113995.

70. Piepenbrink MS, Park JG, Oladunni FS, Deshpande A, Basu M, Sarkar S, Loos A, Woo J, Lovalenti P, Sloan D, Ye C, Chiem K, Bates CW, Burch RE, Erdmann NB, Goepfert PA, Truong VL, Walter MR, Martinez-Sobrido L, Kobie JJ. 2021. Therapeutic activity of an inhaled potent SARS-CoV-2 neutralizing human monoclonal antibody in hamsters. Cell Rep Med 2:100218.

71. Jensen EC. 2013. Quantitative analysis of histological staining and fluorescence using ImageJ. Anat Rec (Hoboken) 296:378-81.

72. Piepenbrink MS, Park J-G, Oladunni FS, Deshpande A, Basu M, Sarkar S, Loos A, Woo J, Lovalenti P, Sloan D, Ye C, Chiem K, Erdmann NB, Goepfert PA, Truong VL, Walter MR, Martinez-Sobrido L, Kobie JJ. 2020. Therapeutic activity of an inhaled potent SARS-CoV-2 neutralizing human monoclonal antibody in hamsters. bioRxiv doi:10.1101/2020.10.14.339150:2020.10.14.339150.

73. Deshpande A, Harris BD, Martinez-Sobrido L, Kobie JJ, Walter MR. 2021. Epitope classification and RBD binding properties of neutralizing antibodies against SARS-CoV-2 variants of concern. bioRxiv doi:10.1101/2021.04.13.439681:2021.04.13.439681.

74. Oladunni FS, Park JG, Pino PA, Gonzalez O, Akhter A, Allué-Guardia A, Olmo-Fontánez A, Gautam S, Garcia-Vilanova A, Ye C, Chiem K, Headley C, Dwivedi V, Parodi LM, Alfson KJ, Staples HM, Schami A, Garcia JI, Whigham A, Platt RN, Gazi M, Martinez J, Chuba C, Earley S, Rodriguez OH, Mdaki SD, Kavelish KN, Escalona R, Hallam CRA, Christie C, Patterson JL, Anderson TJC, Carrion R, Dick EJ, Hall-Ursone S, Schlesinger LS, Alvarez X, Kaushal D, Giavedoni LD, Turner J, Martinez-Sobrido L, Torrelles JB. 2020. Lethality of SARS-CoV-2 infection in K18 human angiotensin-converting enzyme 2 transgenic mice. Nat Commun 11:6122.

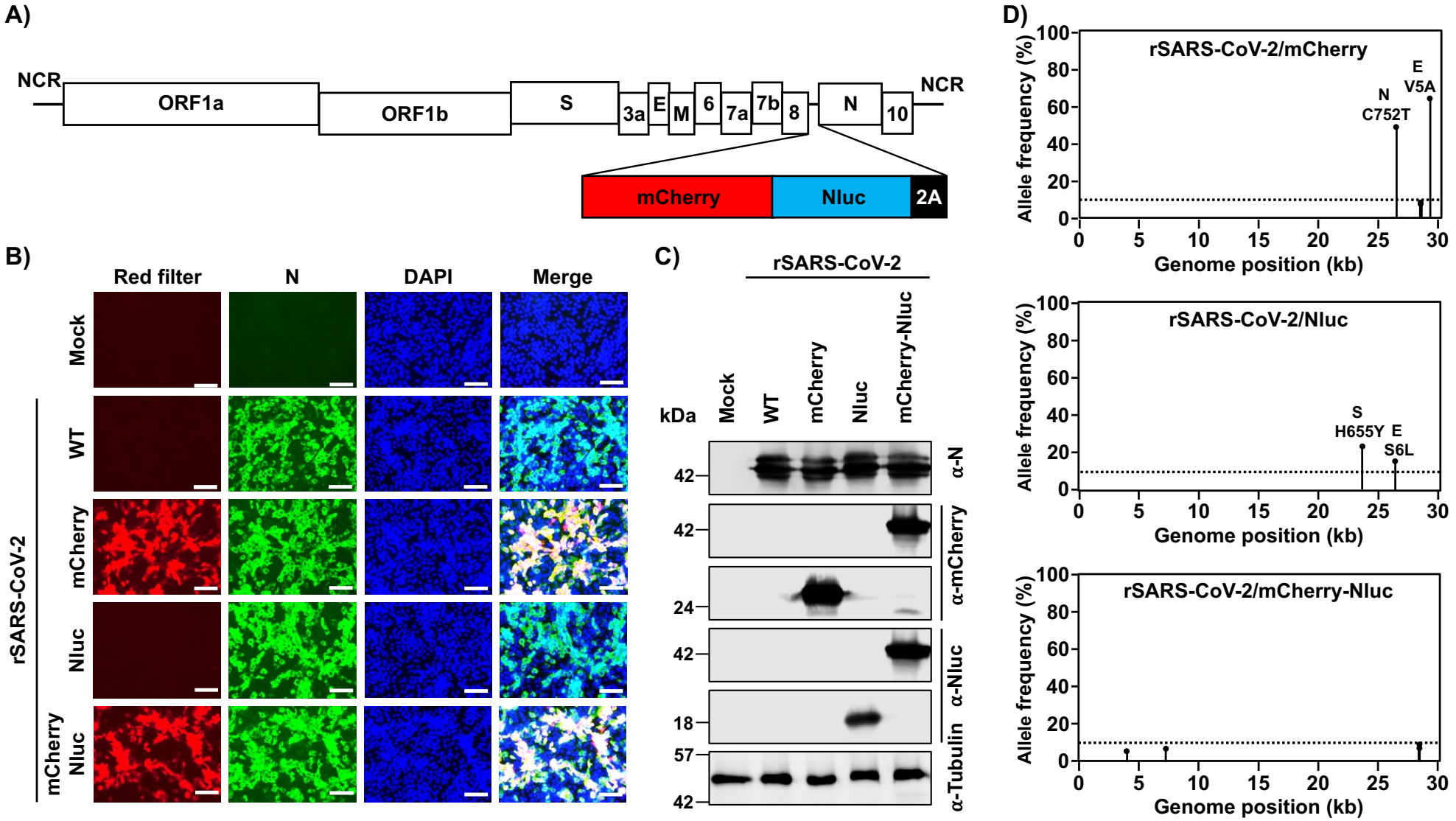
A)
NCR
ORF1a
ORF1b
S
3a
E
M
6
7a
7b
8
N
10
NCR
mCherry
Nluc
2A
B)
Red filter
N
DAPI
Merge
Mock
WT
mCherry
Nluc
mCherry Nluc
rSARS-CoV-2
C)
rSARS-CoV-2
kDa
Mock
WT
mCherry
Nluc
mCherry-Nluc
42
α-N
42
α-mCherry
24
42
α-Nluc
18
57
α-Tubulin
42
D)
rSARS-CoV-2/mCherry
Allele frequency (%)
N C752T
E V5A
Genome position (kb)
rSARS-CoV-2/Nluc
S H655Y
E S6L
rSARS-CoV-2/mCherry-Nluc

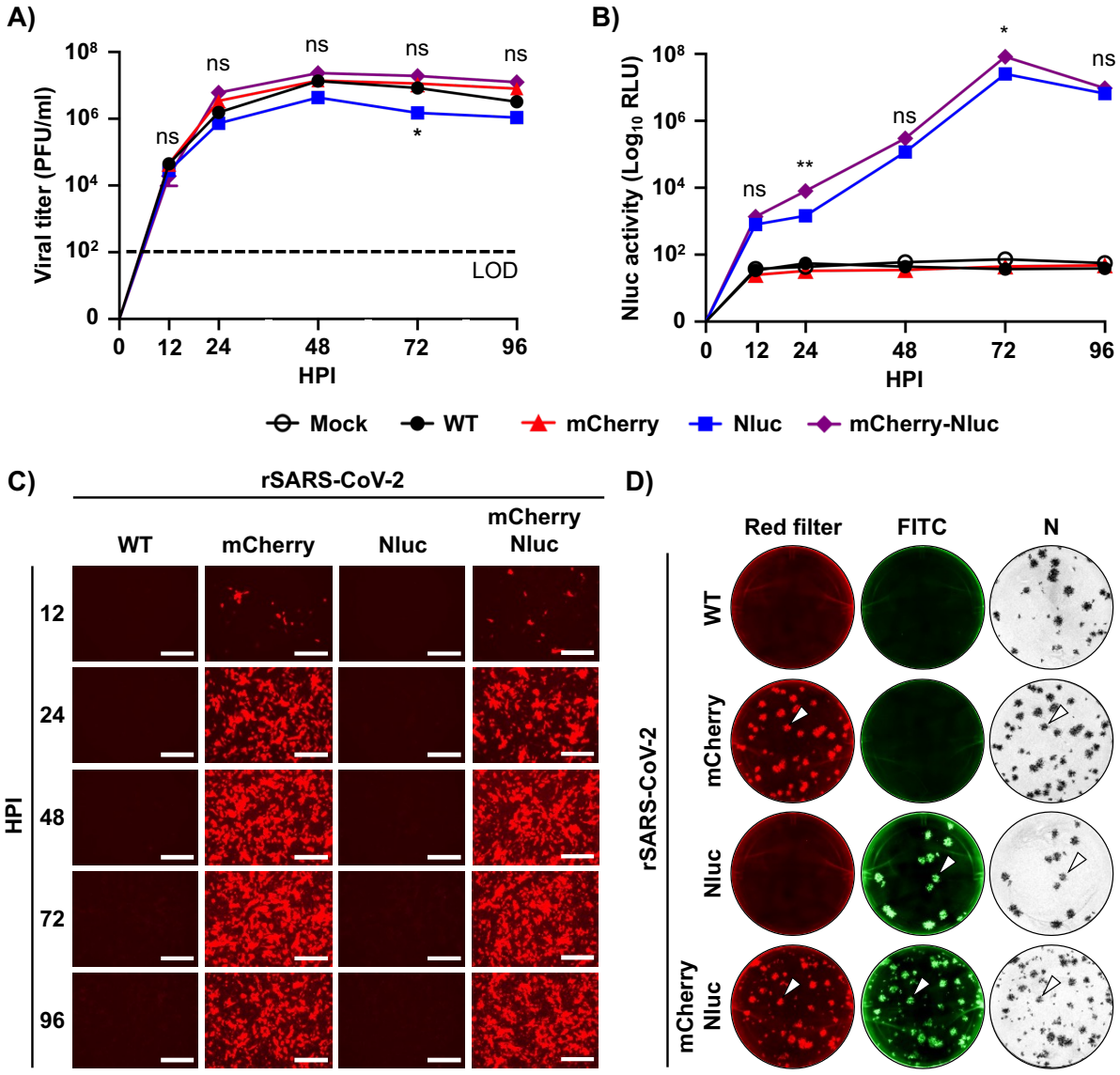
A)
Viral titer (PFU/ml)
10^8
10^6
10^4
10^2
0
LOD
ns
ns
ns
ns
*
0
12
24
48
72
96
HPI
B)
Nluc activity (Log10 RLU)
10^8
10^6
10^4
10^2
0
ns
**
ns
*
ns
0
12
24
48
72
96
HPI
Mock
WT
mCherry
Nluc
mCherry-Nluc
C)
rSARS-CoV-2
WT
mCherry
Nluc
mCherry Nluc
HPI
12
24
48
72
96
D)
Red filter
FITC
N
rSARS-CoV-2
WT
mCherry
Nluc
mCherry Nluc

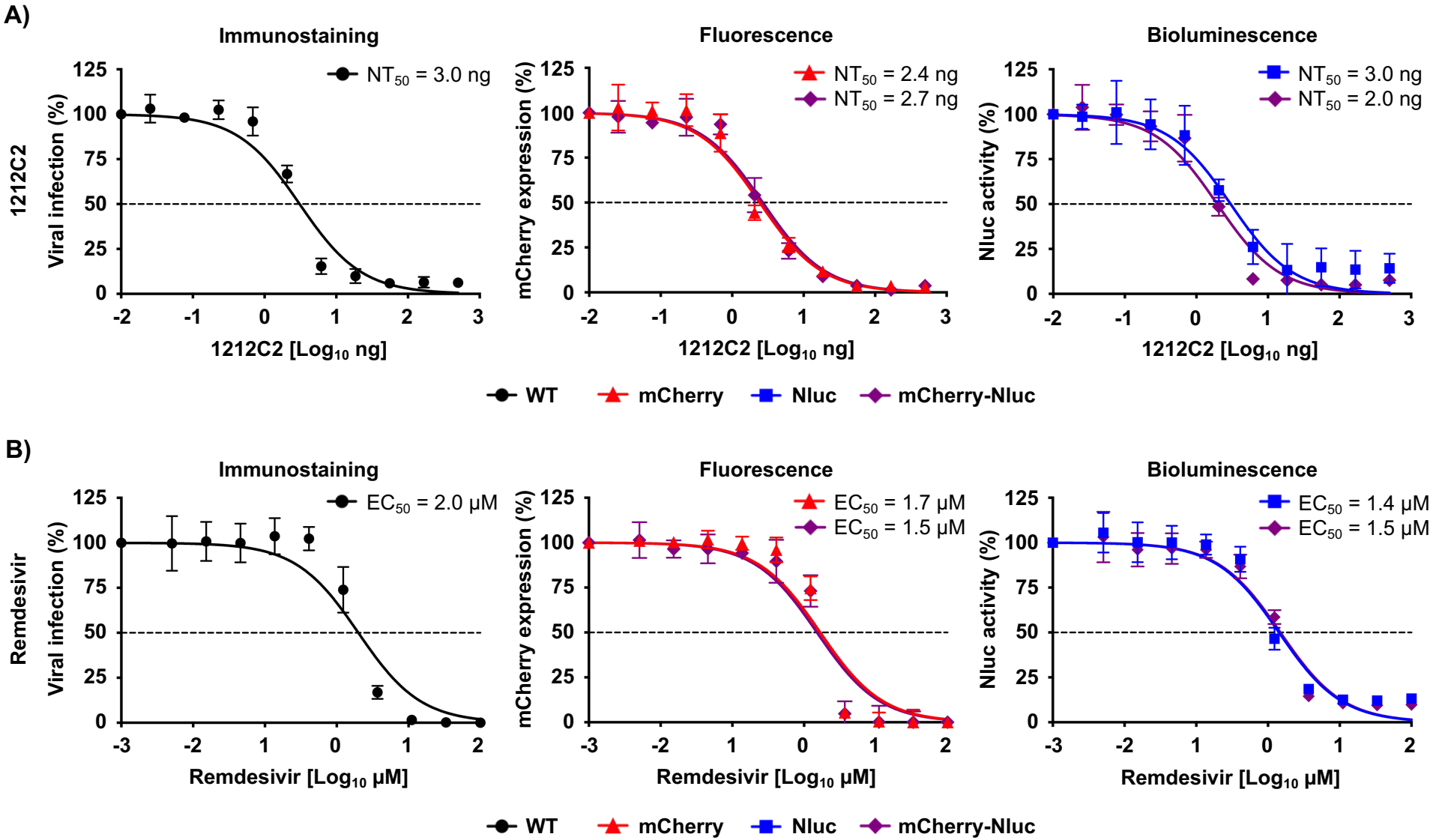
A)
Immunostaining
Fluorescence
Bioluminescence
1212C2
Viral infection (%)
mCherry expression (%)
Nluc activity (%)
NT50 = 3.0 ng
NT50 = 2.4 ng
NT50 = 2.7 ng
NT50 = 3.0 ng
NT50 = 2.0 ng
1212C2 [Log10 ng]
WT
mCherry
Nluc
mCherry-Nluc
B)
Immunostaining
Fluorescence
Bioluminescence
Remdesivir
Viral infection (%)
mCherry expression (%)
Nluc activity (%)
EC50 = 2.0 μM
EC50 = 1.7 μM
EC50 = 1.5 μM
EC50 = 1.4 μM
EC50 = 1.5 μM
Remdesivir [Log10 μM]
WT
mCherry
Nluc
mCherry-Nluc

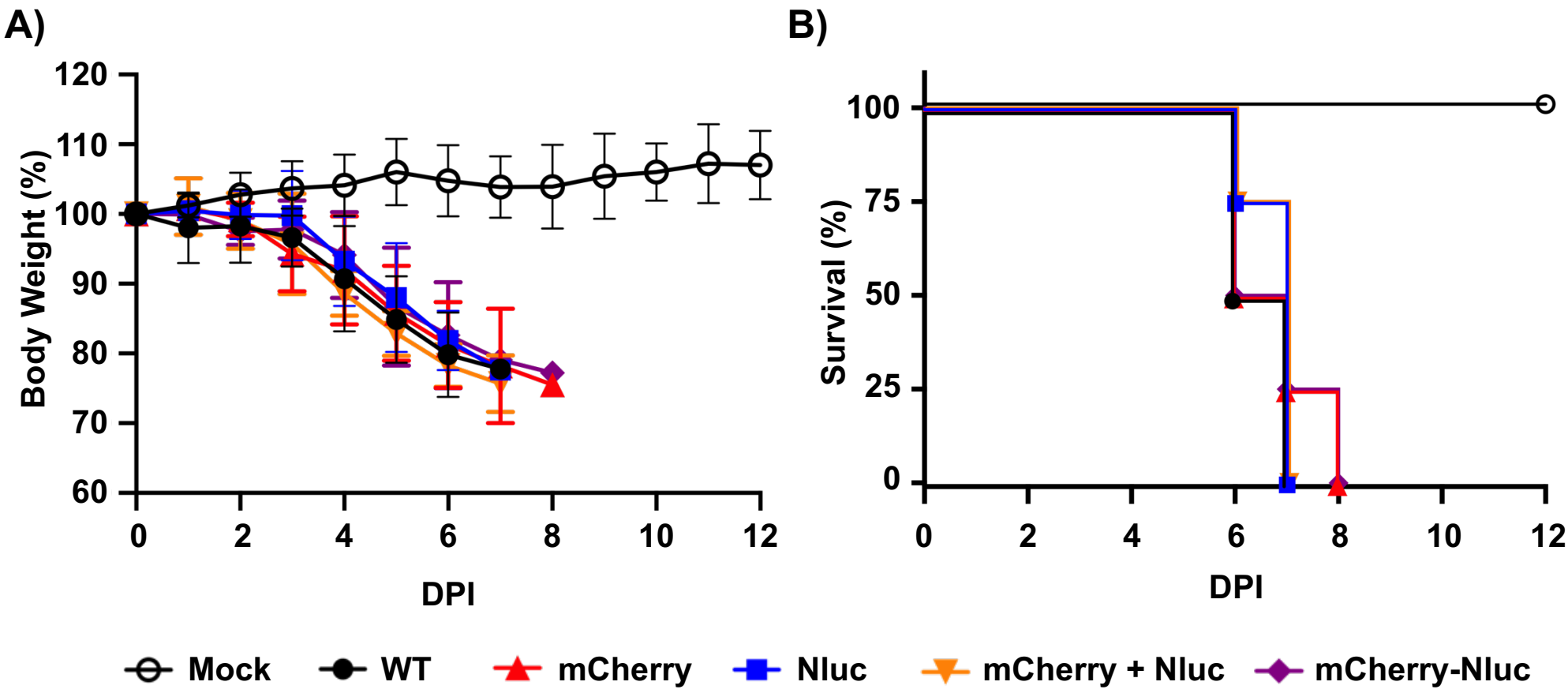
A)
Body Weight (%)
120
110
100
90
80
70
60
0
2
4
6
8
10
12
DPI
B)
Survival (%)
100
75
50
25
0
0
2
4
6
8
10
12
DPI
Mock
WT
mCherry
Nluc
mCherry + Nluc
mCherry-Nluc

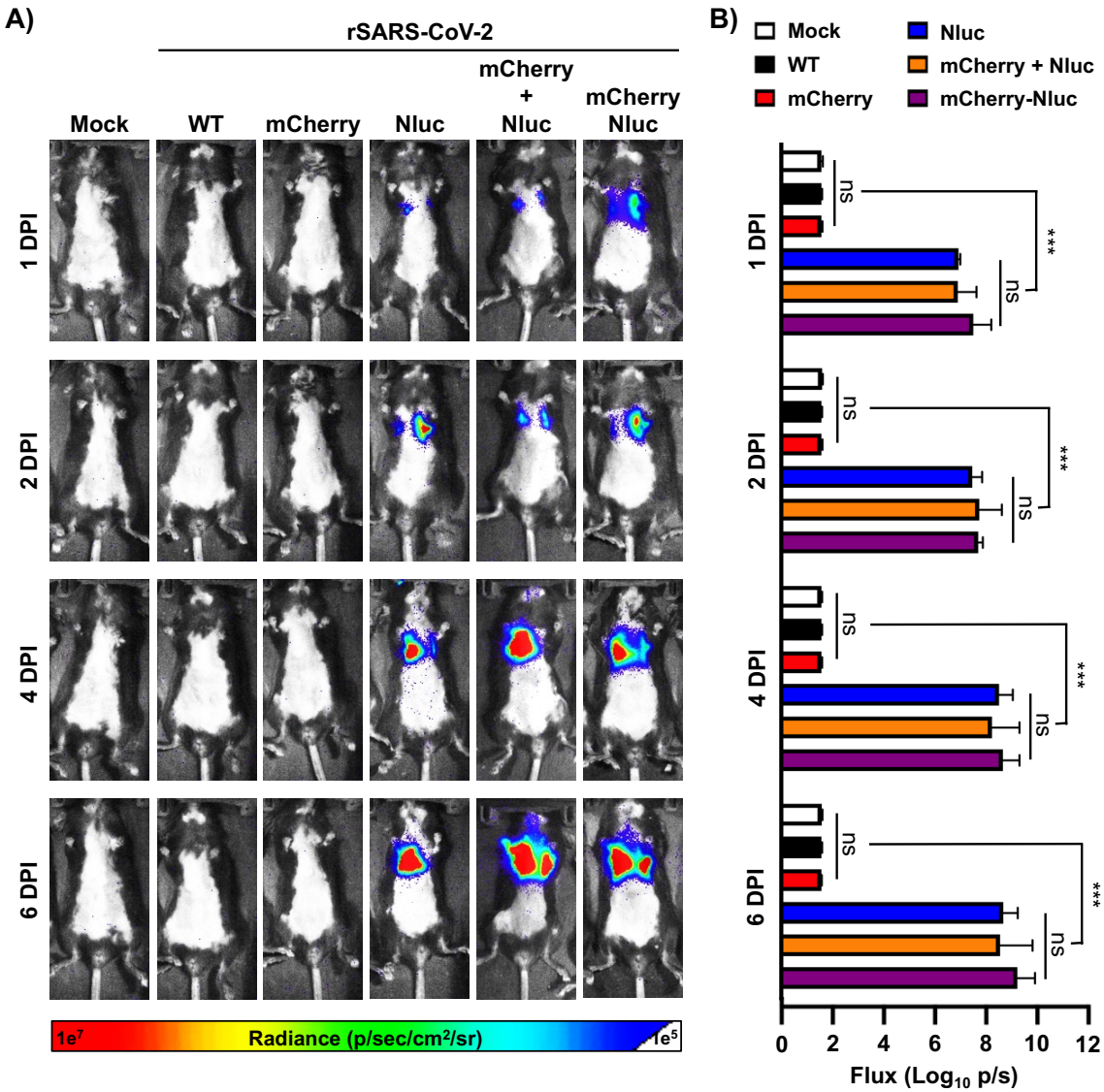
A)
rSARS-CoV-2
Mock
WT
mCherry
Nluc
mCherry + Nluc
mCherry Nluc
1 DPI
2 DPI
4 DPI
6 DPI
1e7
Radiance (p/sec/cm2/sr)
1e5
B)
Mock
WT
mCherry
Nluc
mCherry + Nluc
mCherry-Nluc
ns
***
0
2
4
6
8
10
12
Flux (Log10 p/s)

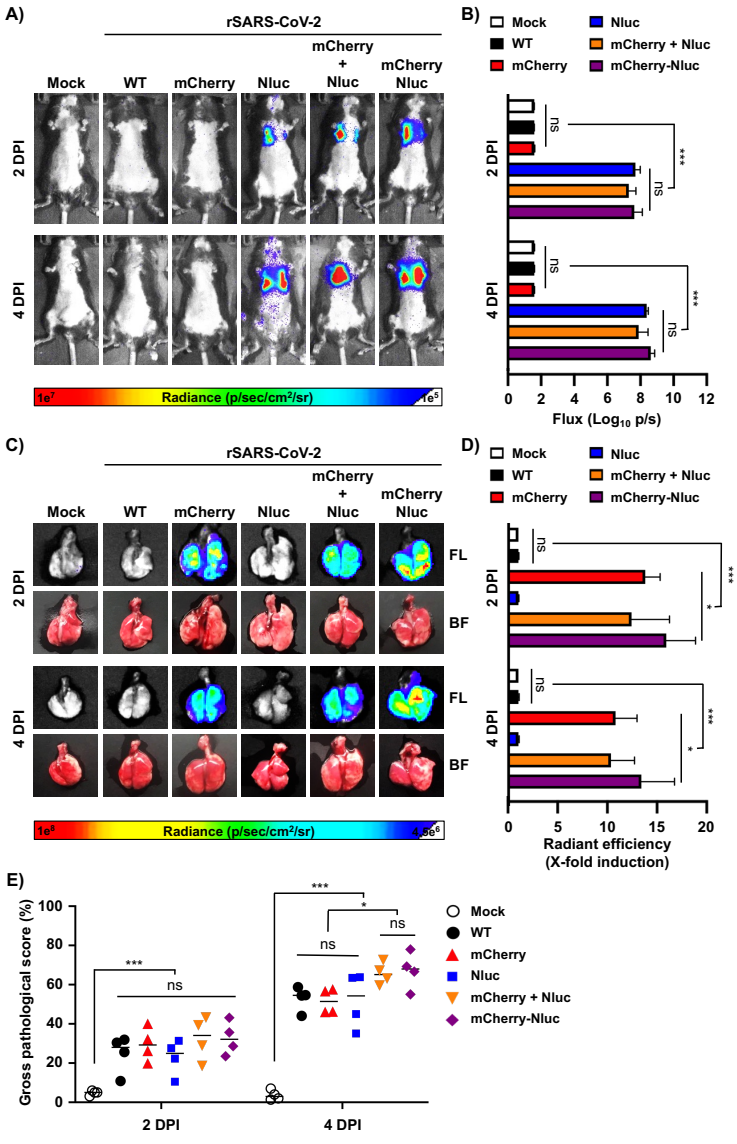
A)
rSARS-CoV-2
Mock
WT
mCherry
Nluc
mCherry + Nluc
mCherry-Nluc
2 DPI
4 DPI
Radiance (p/sec/cm²/sr)
B)
Mock
WT
mCherry
Nluc
mCherry + Nluc
mCherry-Nluc
2 DPI
4 DPI
ns
***
Flux (Log10 p/s)
C)
rSARS-CoV-2
Mock
WT
mCherry
Nluc
mCherry + Nluc
mCherry-Nluc
2 DPI
4 DPI
FL
BF
Radiance (p/sec/cm²/sr)
D)
Mock
WT
mCherry
Nluc
mCherry + Nluc
mCherry-Nluc
2 DPI
4 DPI
ns
*
***
Radiant efficiency
(X-fold induction)
E)
Gross pathological score (%)
2 DPI
4 DPI
ns
*
***
Mock
WT
mCherry
Nluc
mCherry + Nluc
mCherry-Nluc

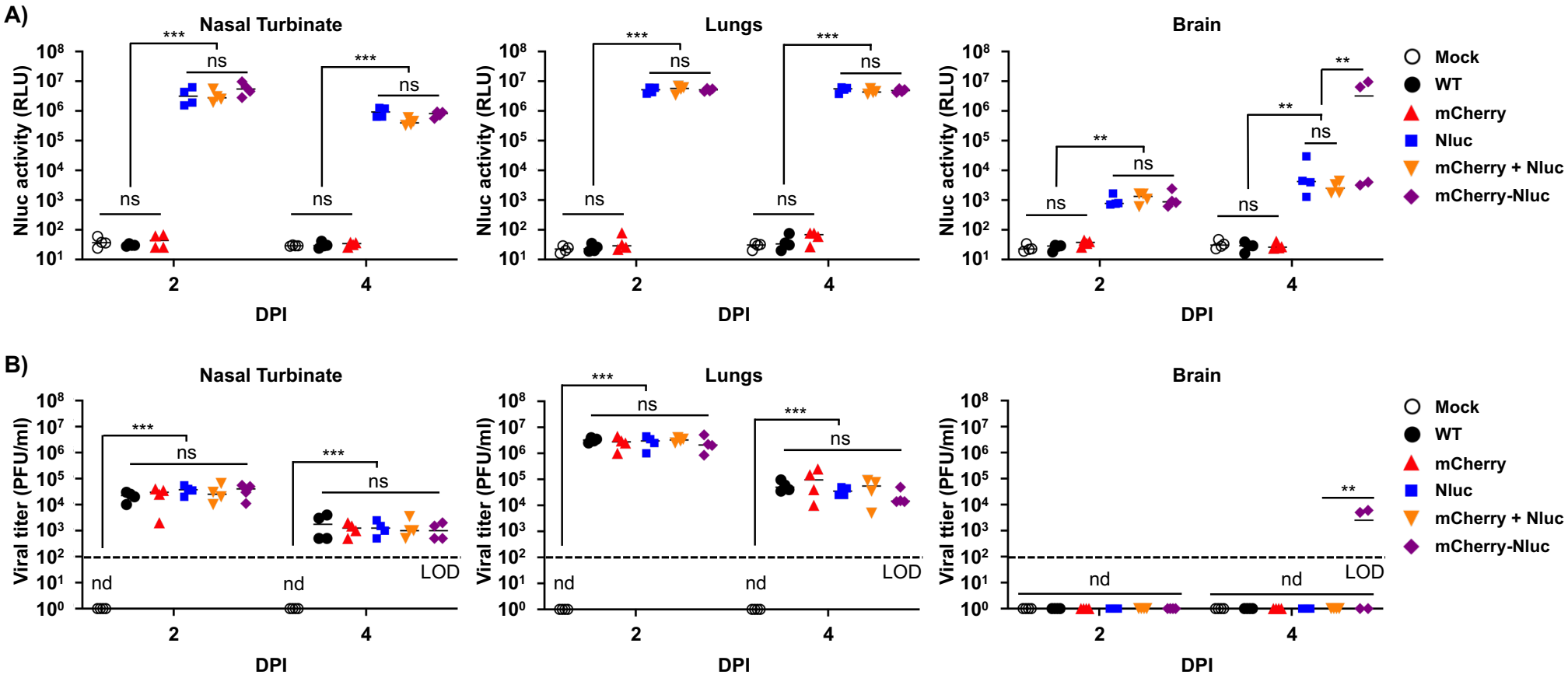
A)
Nasal Turbinate
Lungs
Brain
Nluc activity (RLU)
DPI
ns
***
**
Mock
WT
mCherry
Nluc
mCherry + Nluc
mCherry-Nluc
B)
Viral titer (PFU/ml)
Viral ttier (PFU/ml)
nd
LOD

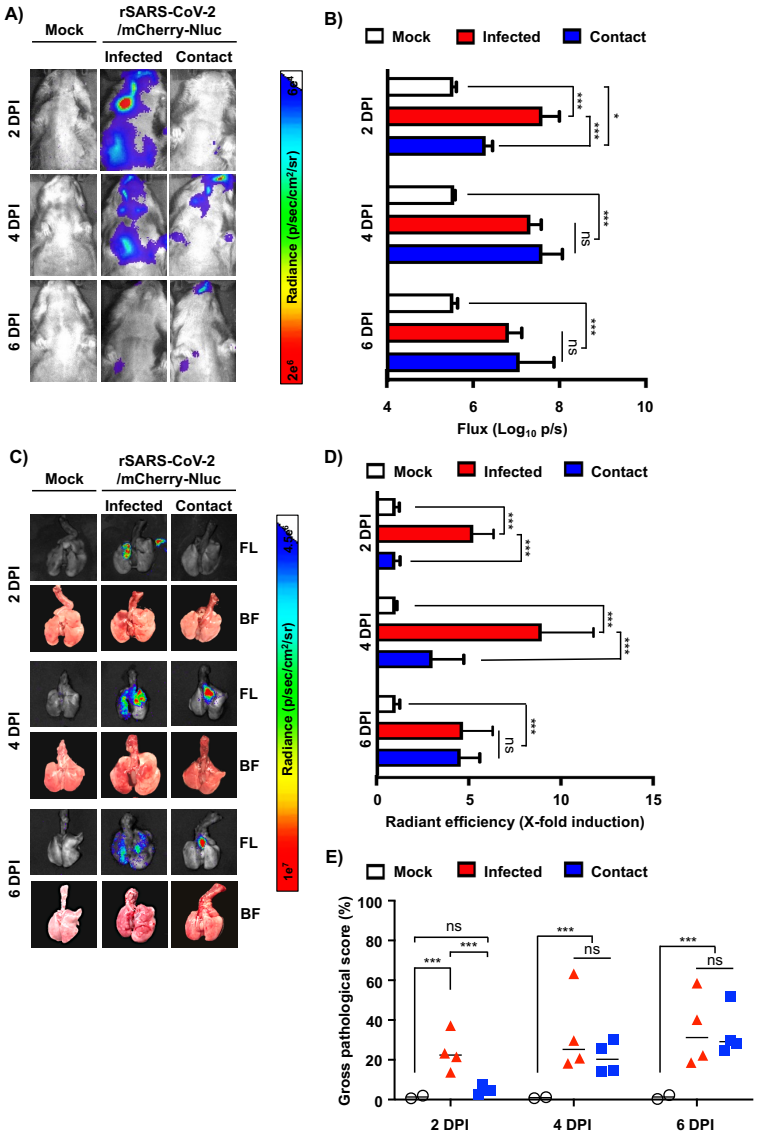
A)
Mock
rSARS-CoV-2 /mCherry-Nluc
Infected
Contact
2 DPI
4 DPI
6 DPI
Radiance (p/sec/cm²/sr)
B)
Mock
Infected
Contact
2 DPI
4 DPI
6 DPI
***
*
ns
4
6
8
10
Flux (Log10 p/s)
C)
Mock
rSARS-CoV-2 /mCherry-Nluc
Infected
Contact
FL
BF
2 DPI
4 DPI
6 DPI
Radiance (p/sec/cm²/sr)
D)
Mock
Infected
Contact
2 DPI
4 DPI
6 DPI
0
5
10
15
Radiant efficiency (X-fold induction)
E)
Mock
Infected
Contact
Gross pathological score (%)
0
20
40
60
80
100
2 DPI
4 DPI
6 DPI

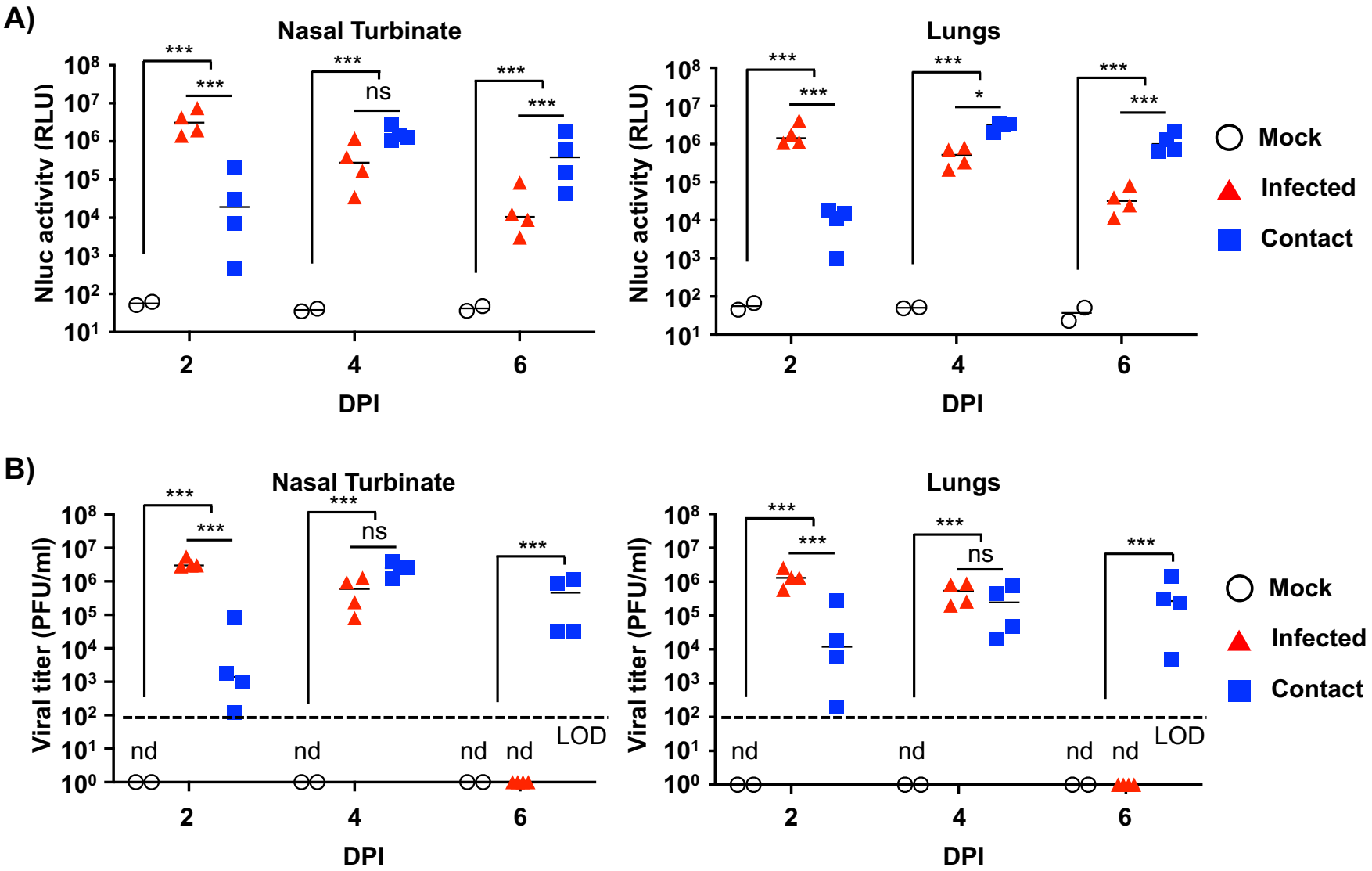
A)
Nasal Turbinate
Lungs
Nluc activity (RLU)
DPI
Mock
Infected
Contact
***
ns
*
B)
Viral titer (PFU/ml)
LOD
nd